

# Monitoring Carbon Dioxide Floods using Electrical Resistance Tomography (ERT): Sensitivity Studies

*A.L. Ramirez, R.L. Newmark, W.D. Daily  
Lawrence Livermore National Laboratory*

This article was submitted to the Journal of Environmental and Engineering Geophysics

U.S. Department of Energy

Lawrence  
Livermore  
National  
Laboratory

**May 27, 2003**

## **DISCLAIMER**

This document was prepared as an account of work sponsored by an agency of the United States Government. Neither the United States Government nor the University of California nor any of their employees, makes any warranty, express or implied, or assumes any legal liability or responsibility for the accuracy, completeness, or usefulness of any information, apparatus, product, or process disclosed, or represents that its use would not infringe privately owned rights. Reference herein to any specific commercial product, process, or service by trade name, trademark, manufacturer, or otherwise, does not necessarily constitute or imply its endorsement, recommendation, or favoring by the United States Government or the University of California. The views and opinions of authors expressed herein do not necessarily state or reflect those of the United States Government or the University of California, and shall not be used for advertising or product endorsement purposes.

This is a preprint of a paper intended for publication in a journal or proceedings. Since changes may be made before publication, this preprint is made available with the understanding that it will not be cited or reproduced without the permission of the author.

# **Monitoring Carbon Dioxide Floods Using Electrical Resistance Tomography (ERT): Sensitivity Studies**

Abelardo L. Ramirez (ramirez3@llnl.gov; 925-422-6909)

Robin L. Newmark ([newmark@llnl.gov](mailto:newmark@llnl.gov), 925-423-3644)

William D. Daily (daily1@llnl.gov; 925-422-8623)

Lawrence Livermore National Laboratory  
P.O. Box 808  
Livermore, Ca. 94550

## **Abstract**

We have conducted a numerical and physical modeling study to evaluate the sensitivity of electrical resistance tomography (ERT) to electrical resistivity changes caused by CO<sub>2</sub> injection and sequestration in geologic reservoirs. We chose the Maljamar CO<sub>2</sub> flood (pilot study) as a basis for our numerical modeling study. We also constructed physical models consisting of blocks of various materials inserted in a water tank to evaluate some of the conclusions of the numerical study. This study quantifies the effects of a variety of factors that affect the resolution and accuracy of the ERT method, under realistic conditions of scale, contrast, and measurement error. It considers scenarios where vertical arrays of point electrodes are used and where metal-cased boreholes are used as long electrodes. Long electrode tomographs provide information such as the shape, location, and lateral extent of the flood. When point electrode arrays or horizontal wells are available, the approximate vertical extent of the flood and coarse estimates of sequestered CO<sub>2</sub> volume may be deduced. Results from physical models support trends observed in the numerical study. Based on this study, we suggest that the ERT method can help confirm the containment of CO<sub>2</sub>.

## **Introduction**

If geologic formations are to be used to sequester CO<sub>2</sub> for long time periods, it will be necessary to monitor the reservoir containing the CO<sub>2</sub>. Monitoring is necessary to confirm the containment of CO<sub>2</sub>, assess leakage paths, and gain understanding into interactions between CO<sub>2</sub>, the formation and formation fluids. Remote methods are preferred, both to minimize disruption and to reduce costs.

Electrical methods are particularly well suited for monitoring processes involving fluids. The electrical properties of geologic systems depend on many of the same factors relevant to CO<sub>2</sub> sequestration. The electrical resistivity and impedance of rocks and soils depend on: water saturation, the amount and type of ions in the water, pH, cation

exchange capacity of the minerals, and on temperature. As a result of these dependencies, high resolution tomographs of electrical properties have been used with success for both site characterization and to monitor subsurface migration of various fluids such as subsurface steam floods, underground tank leaks, water infiltration events, and contaminant movement (Binley et al., 1996, Binley et al., 2001, Daily et al., 1992; Daily et al., 1998; Kemna, et al. 2000, LaBrecque et al., 1996, LaBrecque et al., 1998, Lundegard and LaBrecque., 1995, Newmark *et al.*, 1998, Oldenburg and Li, 1994, Ramirez *et al.*, 1993; Ramirez *et al.*, 1996, Sasaki, 1994, Schima et al., 1996, Slater et al., 1997a, 1997b). Electrical imaging techniques have also been used successfully to monitor the integrity of subsurface barriers (Daily and Ramirez, 2000), and monitor changes in saturation caused by heater tests in welded tuff (Ramirez and Daily, 2001). High-resolution field surveys such as these are typically conducted using subsurface “point” electrode arrays in a cross-well configuration. By “point” electrode we mean that the electrode size is much smaller than the distance separating adjacent electrodes.

Metal-cased boreholes are common in typical oil reservoirs and are electrically conductive. The casings can be used as long electrodes, thus permitting the same infrastructure to have both an operational and a monitoring role. A relatively uncommon strategy in the electrical resistivity imaging method is the use of existing subsurface infrastructure to image the reservoir. Ramirez et al., 1996 and Shi et al., 1997 report on environmental and geothermal studies where steel casings were used as electrodes in combination with point electrodes to produce useful three-dimensional ERT tomographs. Specialized hardware that can produce, measure and switch currents of 10 amperes or higher (at about 100V) is required to use steel casings as long electrodes. In recent field tests using abandoned steel casings in an oil field undergoing steam flood, mapped changes in the electrical properties were found that were consistent with production events (Newmark et al., 1999, 2000). If such imaging can be performed using operational casings as electrodes, this provides a nearly noninvasive method for monitoring the CO<sub>2</sub> injection process, and for verifying the containment of CO<sub>2</sub> within the reservoir.

The objective is to produce time dependent maps of changes in formation resistivity caused by CO<sub>2</sub> injection and migration. Using the existing subsurface infrastructure would require no additional drilling. Vertical wells alone can provide information regarding the lateral changes in a field. If horizontal wells are available, some vertical resolution may be provided as well. ERT surveys can be made in an automated, remote fashion; these capabilities translate into lower costs. The ability to conduct surveys at any time, without disrupting operations, is highly desirable. This is in contrast with conventional cross-well and logging surveys, which often require the removal of pumps and tubing from wells, thereby disrupting injection or production operations. In addition to providing insight into injection/sequestration performance over time, such surveys would provide a context for decisions regarding the deployment of more focused (and more expensive) survey methods such as the high-resolution 3D seismic technique.

### Approach:

The sensitivity and resolution of the ERT method are dependent on a number of factors. These include the type of electrode (point or long), the electrical resistivity contrast between an anomaly and the background, the anomaly location (particularly its proximity to the electrodes), anomaly size and shape, measurement error, and the objective function used by the inversion algorithm. Our sensitivity studies were designed to explore all the above, and to determine the accuracy of CO<sub>2</sub> volume estimates remaining in a reservoir.

Using published field data and unpublished information obtained through communication with industry collaborators, we developed a set of models representing realistic CO<sub>2</sub> injection projects. Numerical simulations were conducted to investigate the range of conditions and measurement configurations under which ERT methods may be used to monitor the changes resulting from CO<sub>2</sub> injection and migration. We also conducted analogous investigations using laboratory-scale, physical models to corroborate key conclusions based on the numerical simulations. We paid special attention to the possibility of using ERT images to estimate the volume of CO<sub>2</sub> remaining in the reservoir; if proved successful, this capability could provide crucial data on the containment effectiveness of the geologic reservoir.

### Numerical Model:

The numerical model used was patterned after a pilot CO<sub>2</sub> flood conducted in an operating oil field. The test is known as the Maljamar pilot, and was conducted in Lea County, New Mexico during the mid 1980s (Albright, 1984). The flooded layers consisted of dolomitic sands and dolomites, located at depths of 1130 and 1230 m. The CO<sub>2</sub> was injected as a supercritical liquid. The layers used for injection were approximately 8 m thick. The pilot flood used a 5 acre (0.02 Kilometer<sup>2</sup>), inverted 5 spot arrangement for the injection/production wells (the center well was used for injection). Two observation wells provided access to the flood zones and were used to conduct a suite of well logs that included induction logs. The induction logs sampled the electrical properties of the layers before, during and after the CO<sub>2</sub> flood. They showed that the resistivity of the layers increased by about a factor of 5 during the CO<sub>2</sub> flood.

We constructed a numerical model with electrical properties similar to those of the Maljamar pilot. In our model, we assume that CO<sub>2</sub> is injected into a single 14 m thick layer located at depth. The pre-flood resistivity of the layer is 10 ohm-m. In the numerical modeling, a number of factors known to affect the sensitivity and resolution of ERT were varied. These factors include resistivity contrast, the anomalous body size, shape and proximity to electrodes, measurement error, and electrode deployment.

A 9 spot, 20 acre pattern of wells was selected to simulate realistic oil-field scales. The wells surround a block that is 285 m by 285 m (horizontally), with well spacing equal to 142 m. The model considers three electrode deployment patterns:

- a) 9 vertical wells, with 10 “point” electrodes in each
- b) 9 vertical steel casings used as long electrodes

c) 9 vertical and 6 horizontal steel casings, all used as long electrodes.

Although the “point” electrode deployment is expected to provide the highest resolution, the relatively large spacing between electrodes (28.4 m vertically, 142 m laterally) makes this measurement configuration quite coarse relative to the more common environmental applications of the method. However, this larger spacing is more representative of realistic deployment options in an oil field. For all models, we assumed a 4 electrode measurement scheme using the dipole-dipole configuration.

Another reasonable deployment may involve the use of surface electrodes together with long electrodes to image the subsurface. Preliminary modeling of this scenario suggested that the surface electrodes did not contribute significantly to the resolution or sensitivity of the method. We believe that this is due to the large distance between surface electrode and the reservoir. For this reasons this scenario was not considered. For shallower applications, this approach may prove to be useful.

Figure 1 depicts the three deployment options used and the resistivity model corresponding to the pre-flood or baseline case. The pre-flood resistivity of the layers was set to 10 ohm-m surrounded by a 100 ohm-m background. To simulate the effects of CO<sub>2</sub>, the electrical properties of the center layer in Figure 1 were changed as follows: flood layer, initially at 10 ohm-m, changed to 100, 50, 20, 15, 13, 11, or 2 ohm-m. These resistivity values translate into changes ranging from +900% to –80%. Note that this range includes the +400% change (five-fold increase) observed during the Maljamar pilot as well as smaller changes; we also considered resistivity decreases (five-fold-decrease or –80%). The smaller changes allow us to study the lower limits of sensitivity for the technique.

We tested 6 anomaly shapes, designed to model expected distribution of CO<sub>2</sub>; Figure 2 illustrates their shapes, positions, and volumes. These include:

- 1) 3 horizontal tabular bodies, positioned at different locations relative to the center well in the 9 spot pattern,
- 2) a narrow “finger” anomaly simulating a preferential flow path within the layer, and,
- 3) vertical penetrations originating from an initial horizontal tabular body, simulating a vertical breach of the caprock above the reservoir unit. We assume that caprock CO<sub>2</sub> penetration causes the same relative change in electrical resistivity as CO<sub>2</sub> penetration of the reservoir.

#### Physical Models:

We used physical models to evaluate the validity of some of the key conclusions suggested by the Maljamar numerical study. The volume estimates based on physical models were compared with estimates of CO<sub>2</sub> volume calculated for the numerical simulations. Other issues such as the accuracy of the images were also investigated. The physical models used for the point electrode and long electrodes studies are shown in Figure 3.

The point electrode model consisted of 4 vertical electrode arrays, each having 15 electrodes (drawings on the left side of Figure 3). The arrays were submerged in water and a variety of solid plastic and porous (foam) targets having different electrical resistivities were inserted between the electrodes. The water resistivity was 250 ohm-m, the two foam targets had resistivities of 340 and 800 ohm-m, and the plastic resistivity was approximately  $10^{10}$  ohm-m. For each material type, we constructed four targets of increasing volume by using between one and four blocks grouped together.

The long electrode model consisted of 9, 0.64 cm diameter stainless steel rods (drawings on right side of Figure 3). The apparatus was submerged in the water and the same target materials described previously for the point electrodes were also used for the long electrode study.

Forward modeling and inverse reconstruction:

Using this suite of models, the forward problem was solved using a 3D, finite difference technique described by LaBrecque et al. (1999). We use the finite difference method with rectangular, hexahedral elements to convert the potential differential equation into a system of linear equations. Within each element, electrical conductivity is constant. The algebraic equations produced by the finite difference method are of the form:

$$\underline{G}V = I \quad (1)$$

where  $\underline{G}$  is an M by M matrix, V is a vector of the estimated potential at nodes, I is a vector of the current injected at electrode locations, and M is the number of mesh nodes.

Highly conductive structures such as metallic casings are modeled by lowering the conductances in the matrix  $\underline{G}$  (eq. 1) along columns (or rows) of nodes in the finite difference mesh. The value of the conductances between such nodes is calculated using the diameter and electrical resistivity of the casing material. The modified conductance values remain fixed during inversion. We used this algorithm to calculate electrical resistance data for various models. The calculated data were corrupted by adding to it noise sampled from a uniformly random distribution (+/- 2%). The inverse problem was then solved using the corrupted data.

We also used the three-dimensional inverse algorithm described by LaBrecque et al. (1999). Three-dimensional inversion is by nature strongly underdetermined. Inverse solutions that consider only the fitting of the forward model to field data are non-unique. Therefore, the algorithm uses a regularized solution (Tikhonov and Arsinen, 1977) that jointly minimizes the misfit of the forward model to the field data and stabilizes the inverted value of the parameters. To find the optimal value of the parameter vector  $\mathbf{P}$ , the algorithm finds the maximum value of  $\alpha$ , the stabilization parameter, for which minimizing:

$$Y(\mathbf{P}) = \chi^2(\mathbf{P}) + \alpha \mathbf{P}^T \underline{R} \mathbf{P} \quad (2)$$

results in:

$$\chi^2(\mathbf{P}) = \chi_{prior}^2. \quad (3)$$

The parameters,  $\mathbf{P}$ , are the natural logarithms of the conductivity of the mesh elements. In equation 2, we use  $\mathbf{R}$ , the solution roughness, as the stabilizing functional. Also in equation (2),  $\chi_{prior}^2$  is equal to the number of data points and  $\chi^2$  is given by:

$$\chi^2 = (\mathbf{D} - \mathbf{F}(\mathbf{P}))^T \mathbf{W} (\mathbf{D} - \mathbf{F}(\mathbf{P})) \quad (4)$$

where  $\mathbf{D}$  is the vector of known data values,  $\mathbf{F}(\mathbf{P})$  is the forward solution and  $\mathbf{W}$  is a data weight matrix. The diagonal elements of  $\mathbf{W}$  are the reciprocals of the data variances and the off-diagonal elements are zero. This assumes non-correlated data errors.

We note that for a given  $\alpha$ , usually one  $\mathbf{P}$  vector will yield the desired  $\chi_{prior}^2$ . This means that the approach can produce a unique solution given the roughness parameter used. The roughness operator  $\alpha$  controls the relative weighting of roughness (the inverse of smoothness) and data fitting in the objective function. It helps stabilize and remove ambiguity in the resistivity inversion by minimizing the model roughness (maximizing model smoothness). This operator in a very real sense trades off resolution and sensitivity for inversion robustness. This means that the inversion process can be tuned to be very robust or to fit the data very accurately, but both goals cannot be accomplished equally well at the same time. In actual practice, the  $\alpha$  estimator used aims to achieve a balance between these two goals. In typical problems, it produces resistivity models that exhibit minimum roughness while fitting the data to a prescribed prior tolerance specified by  $\chi_{prior}^2$ .

## Results - Numerical Model

### Point Electrodes:

We first focus on the sensitivity and resolution obtained for the Maljamar numerical model, point electrode scenario. The top half of Figure 4 shows the tomographs obtained for a tabular target embedded within the middle layer near the center of the the Maljamar model. The lower half of the figure shows the results for a “finger”-like anomaly. The tomographs show the reconstructed percent changes in resistivity between the baseline model and the model with the embedded target. Parts of the volume are rendered transparent so that we can look inside it. The transparency threshold is based on the magnitude of the resistivity change. For example, for those tomographs labeled as transparent from –20 to 20%, any part of the tomograph that contains changes outside the range is rendered opaque, and the rest of the volume is rendered transparent.

For target contrasts larger than 50% (i.e., targets with a resistivity equal to or greater than 15 ohm-m embedded in a layer of 10 ohm-m), and for transparency levels of +/- 20%, the location and size of the tabular target are reasonably close to the model. The square target is reconstructed as a rounded structure with a resistivity contrast that is lower than the



true contrast. These distortions are probably caused by the regularization approach used by the inversion algorithm. For a transparency level of  $\pm 10\%$ , the tabular target can be seen for contrasts as low as 30%; however, the tomographs also show artifacts (features unrelated to the target). The maximum value for these artifacts is between 15 and 20%. This means that, given the model parameters and noise levels assumed, we can reliably interpret changes greater than 15-20% as being related to the target; changes below that could conceivably be caused by measurement noise and numerical modeling error.

Similar comments can be made regarding the “finger” target in the lower half of Figure 4. This target is more difficult to reconstruct than the tabular target discussed above because it is significantly smaller and it is relatively thin in two directions instead of one. As a result, the distortions due to the smoothing kernel are likely to be more severe. For target contrasts larger than 100% and for transparency levels of  $\pm 20\%$ , the location and size of the tabular target are reasonably close to the model. Artifacts can also be observed at transparency levels of  $\pm 10\%$ .

We now focus our attention on targets that changed the baseline resistivity by a factor of +400%, (target is five times more resistive than the baseline condition). This is the level of change detected by induction logs during the Maljamar pilot CO<sub>2</sub> flood. The images on the top half of Figure 5 present the results obtained for all the targets considered. Questions that a reservoir manager might ask are, “Is it possible to map the reservoir regions invaded by the CO<sub>2</sub> flood?” and, “Is the flood following a preferential flow path(s)?”. These questions can be answered by comparing the results for models L1, L2, and L3. Let us assume that the center well in the nine-spot pattern is a CO<sub>2</sub> injection well. Model L2 consists of target that is approximately centered while the L1 model is displaced from the center. The L2 image clearly shows the target approximately centered while the L1 image shows it away from center, as it should be. The L3 image suggests that a preferential flow path has developed. These results suggest that the images can be used to infer what parts of the reservoir are accepting the flood, and which areas have been bypassed.

Another question that a reservoir manager might ask is: “Can the images reliably detect CO<sub>2</sub> escaping the reservoir through the caprock?”. This question can be answered by comparing the results for models L4, L5, and L6 (top half of Figure 5). Models L4 and L5 contain a pillar that extends into the layer overlying the reservoir layer. This pillar simulates a caprock breach. The images corresponding to L4 and L5 show only very subtle indications of this pillar. In fact, they look very similar to the L6 image, which represents the same tabular model without the pillar. We conclude that it is unlikely that these images can be used to identify the caprock breach in our model. The reader is reminded that the electrode spacing is relatively large compared to the dimension of the features of interest. If the distances between electrode arrays (or individual electrodes in the arrays) are reduced, the ability to resolve a breach can be improved significantly.

One possible reason for the lack of sensitivity to the pillar is that the caprock is ten times more resistive than the reservoir layer, and the CO<sub>2</sub> pillar increases its resistivity even more. This means that relatively little current gets to the pillar, thereby reducing the

sensitivity to it. The images in the lower half of Figure 5 can be used to evaluate this hypothesis. These images show the reconstructed changes for targets that are a factor of five less resistive than the baseline case. Note that the L4 and L5 images show a more recognizable thickening at the pillar location, and that there is larger difference relative to the L6 image. This means that the conductive pillar in our model would be somewhat easier to detect than a resistive pillar. However, even a conductive pillar would be poorly resolved.

The rest of the images on the lower half of the figure are very similar to the corresponding images when resistivity increases (upper half of the figure).

#### Vertical Long Electrodes:

The benefit of using long electrodes is that existing steel-cased boreholes can be used for monitoring, thereby dramatically reducing costs. This benefit comes at the expense of sensitivity and resolution. In this section, we look at the long electrode tomographs from the Maljamar numerical model to evaluate their sensitivity and resolution. The nine, vertical long electrodes were arranged in a nine-spot pattern, as shown in Figure 1.

Figure 6 shows the long electrode tomographs for targets L1 to L6. The top half of the figure shows the results calculated when the target resistivity is 5 times higher than background. The bottom half of the figure shows the results obtained when the target resistivity is 5 times lower than background. Horizontal projections of the targets have been superimposed to facilitate comparison to the “truth”. These tomographs can be compared to the point electrode tomographs in Figure 5.

First, we note that the long electrode tomographs have no vertical information. As a result, a single slice through the medium is sufficient to analyze the tomograph because all horizontal slices would look identical. The lack of vertical resolution eliminates the possibility of detecting caprock breaches by the CO<sub>2</sub> and the possibility of estimating volume. Second, there is sufficient resolution to approximately locate the position of the target in the horizontal plane. For example, there is a clear difference in the position of the anomalies for tomographs L1, L2, and L6. There is also enough resolution to distinguish between the tabular targets and the “finger” target. The magnitude of the changes observed is substantially less than changes observed using point electrodes. For example, the magnitude of the change observed for the “finger” target (L3 image, 400% contrast, top row of images in Figure 6) ranges from 1 to 4.5%; the corresponding change for the point electrode case ranges from 23 to 66%. This reduced sensitivity is due to the fact that long electrode measurements integrate the electrical resistivities along their entire length. Consequently, resistivity changes occurring in a layer with a thickness that is about 1% of the total casing length (as in the Maljamar model), are greatly reduced in magnitude.

These results suggest that long electrode tomographs can provide useful information about the horizontal position, size, and shape of the region invaded by the CO<sub>2</sub> flood. Compared to point electrode tomographs, long electrode tomographs show lower resolution and substantially lower sensitivity. These results confirm our prior hypothesis

that using steel-cased production and injection wells as long electrodes carries a tradeoff between cost and decreased sensitivity and resolution.

#### *Horizontal and Vertical Long Electrodes:*

In the previous section, we proposed that vertical long electrodes produce images with no vertical information. The leftmost figure in Figure 7 illustrates why this is. The image shows the current density field produced by two adjacent steel wells. We choose to plot current density because it is proportional to potential gradient magnitude. The dimensions on this image are identical to the dimensions of the Maljamar model. The image shows that there are large horizontal potential gradients, and negligible vertical potential gradients. This means that: 1) almost all current is flowing horizontally, and 2) the direction of current flow is controlled by the casing orientation. Casings of different orientations should produce different current flow directions. This is shown by the right image in Figure 7 where adjacent horizontal and vertical casings were energized. The figure shows that vertical and horizontal potential gradients are clearly present, thereby implying vertical and horizontal current flow. Using casings of varying orientations may offer the possibility of achieving coarse vertical and lateral resolution. Some reservoirs have steel-cased, horizontal production wells that could be used as long electrodes. We investigated the possibility of using a combination of vertical and horizontal long electrodes in order to achieve both lateral and vertical resolution.

The model consisted of 9 vertical and 6 horizontal wells as depicted by the lower diagram in Figure 1. The model does not consider the portion of each casing that connects the horizontal section to the surface. This omission simplifies the model but does not compromise the conclusions of this part of the study. The target contrast assumed for this model is +400%.

In Figure 8, a comparison of the results obtained using the three electrode deployment scenarios examined in the Maljamar numerical study is presented. We compare the results for the L1 model when the center layer resistivity changes from 10 to 50 ohm-m. The upper-left image (A) shows the model. The upper right image (B) shows the results obtained when the point electrode arrays are used. Image C, on the lower left of the figure, shows the results obtained when 9 vertical steel-cased wells are used. Image D, on the lower right of the figure, shows the results obtained when 9 vertical and 6 horizontal steel-cased wells are used.

Image C clearly shows that the vertical casing results can only be used to map the lateral position and extent of the target. Image D shows that, when horizontal well data is added, the vertical position and approximate thickness of the target can be recovered. A comparison of images B and D suggests that the results are similar. However, the thickness of the anomaly is more exaggerated in D and the resistivity change in D is weaker than in C.

For the case of the “finger” model (L3 model in Figures 5 and 6), the difference between the “point” electrode and long electrode results are more substantial. In this case, the “point” electrode results are clearly superior.

In summary, coarse lateral resolution should be possible when using vertical steel casings as long electrodes. When both vertical and horizontal steel casings are used, coarse lateral and vertical resolution may be obtained.

#### *Analysis Of Image Fidelity - Point Electrodes:*

The previous discussion has focused on qualitative analysis of the images. A quantitative analysis of the method's reliability is also important, because in many applications we wish to convert the resistivity values to other parameters such as water saturation or the resistivity of the pore fluid. To estimate the reliability of such conversions, it is necessary to characterize the reliability of the reconstructed resistivity values. Here, we limit the analysis to "point" electrode models.

Figure 9 can be used to evaluate the influence of voxel position on the magnitude of the resistivity change recovered by the tomographs. Here we consider a centered tabular anomaly that is relatively easy to resolve (model L1 in Figure 2), and a narrow "finger" anomaly (model L3 in Figure 2) that presents a more difficult challenge. The graphs on the left side of Figure 9 compare the "true" percent resistivity change (in the model) to the recovered percent resistivity change in the tomograph for the various magnitudes of resistivity change considered. The top graph corresponds to the tabular anomaly and the bottom to the "finger" anomaly. Horizontal slices through the 3D mesh are shown on the right hand side of the figure. These slices show the location of the anomalies in the mesh (darker gray areas), the location of the point electrode arrays (white circles), and the location of the voxels to be examined. The symbols on the graphs (square, triangle, and diamond) also appear in the mesh slices to indicate the correspondence between graph values and mesh location.

We first consider the tabular anomaly in Figure 9. The corresponding graph shows a line that indicates "perfect" matching between model and tomograph values. The square symbols come closest to the line. This symbol represents a voxel within the region occupied by the anomaly and near the central electrode array. The triangle symbol identifies a voxel at the edge of the anomaly and farther removed from the electrode arrays. For this voxel, the values in the tomograph are much smaller than values in the model. There are two causes for this behavior. One is that the method's sensitivity to any given voxel value depends on the distance between the voxel and the electrode arrays. A second reason is that the inverse algorithm makes use of a smoothness-constrained, least-squares technique that searches for models having minimal contrast between adjacent voxels. This technique "smears" the resistivity value in a given voxel to adjacent voxels. Thus, the algorithm produces models that tend to under-predict resistivity values in voxels that are some distance away from the electrodes. The last voxel, the diamond symbol, is outside the anomalous region and nearly equidistant from the electrode arrays. It shows very little resistivity change, as expected.

Now consider the results corresponding to the "finger" anomaly in Figure 9. Again we can see that the voxel closest to an electrode array (square symbol) comes closest to the "perfect match line". The voxel identified by the diamond symbol is within the anomaly,

but farther removed from the electrode arrays, and thus under-predicts the apparent resistivity change to a larger extent. These observations are similar to those for the tabular anomaly. However, the under-prediction of resistivity values is more pronounced for the “finger” anomaly. This is probably due to the fact that it has a significantly smaller volume and it is harder to detect than the tabular anomaly.

Similar comparisons between reconstructed and model values are presented in Figure 10. The top plot compares the observed volume within the anomalous zone (zone that is changing in resistivity) to the true model volumes (in ratio form). These volume ratios are presented as a function of target and contrast. The volume we considered here is the volume of the anomaly itself, not the volume of fluid within the anomaly (fluid volumes will be discussed later). To calculate the volume of the anomaly, we summed the volume of all voxels with a resistivity change equal to or greater than 10%; in other words, we arbitrarily assumed that changes above 10% were reliable. The plot curves suggest that volume is generally over-predicted (volume ratios greater than one). Also, the volume ratios increase with the magnitude of resistivity change. For 400% resistivity change, the anomaly volume is 7 to 10 times larger than the model volume for all but one target; for the L3 (“finger”) target the anomaly volume is about 16 times larger.

We believe that these over-predictions are a direct result of the regularization approach used by the inversion algorithm that searches for “simple” (smooth) models. Thus, an important consequence of this approach is that the predicted resistivity and volume are distorted but behave in such a way that the predicted change in resistance (i.e., predicted resistivity \* predicted volume) approximately equals the actual change in resistance.

The bottom plot in Figure 10 compares the average resistivity change within the anomalous zone to the true model change (in ratio form). The curves suggest that the average resistivity change is generally under-predicted (ratios less than one). Resistivity change is increasingly under-predicted as the true resistivity change increases in magnitude. For 400% resistivity change, the resistivity change predicted is about 10 times smaller than the true change. We believe that these distortions are also caused by the regularization used.

In summary, the tomographs generally over-predict the volume of the region undergoing change and under-predict the magnitude of the resistivity change. In doing so, the inverse algorithm produces a resistivity structure that offers approximately the same level of resistance to current flow as the true target.

#### Measurement error –Point electrodes:

We examined the effects of measurement error on the reliability of the tomographs. Specifically, we evaluated the influence that measurement error magnitude has on the reliability of reconstructing small resistivity changes. We also considered the effects that noise correlated in time may have on resistivity change images. Uniformly distributed random number sets were used to corrupt the data. For some of the simulations, the “pre-flood” and “during flood” data sets were corrupted using different sets of random numbers. For other simulations, the “pre-flood” and “during flood” data sets were

corrupted using the same random number set in order to simulate noise that is correlated in time.

We first discuss the influence that noise magnitude may have on the images. Figure 11 shows the results of simulations where different levels of noise were added to the data. We chose the “finger” anomaly, because it is the smallest and most difficult one to detect. Simulations for the other targets showed better results overall. The top row shows the results when 2% noise was added to the data and the inversion algorithm assumed that the data uncertainty as indicated by the standard deviation was 2%. In our experience, 2% measurement errors are typical of most ERT surveys. Note that, for the case of 30% change in model resistivity, pieces of the “finger” anomaly can be seen. However, other regions of the image show changes that are just as significant. When the resistivity change is only 10%, the finger anomaly is unobservable.

The bottom row of images in Figure 11 shows the results when 0.2% noise was added to the data and the inversion algorithm assumed that the standard deviation of the data was 0.2%. This level of noise is unusually low; however, it may be achievable in the field by such means as stacking the data for longer periods of time, increasing the received voltages by increasing the transmitted current, and by using low-noise electrodes. The bottom row of images shows that the finger anomaly can be resolved for both magnitudes of resistivity change. These results suggest that measurement error can have a significant influence in situations where the magnitude of change is small and the anomaly is relatively small in volume. For situations where the magnitude of change and the anomaly size are relatively large, the magnitude of the measurement error had an insignificant effect on the anomalies. Our analysis also suggests that very similar tomographs are obtained regardless of whether the noise is correlated in time or not.

When different 2% random noise sets were added to simulations (resistivity increases of 400%) and the resulting tomographs were compared, we made the following observations. The tomographs show that voxels located away from the anomaly had differences as much as 10%. By contrast, the differences were found to be about 2% for voxels within the anomaly. This means that voxels exhibiting large resistivity changes are relatively unaffected by measurement error, and voxels exhibiting negligible resistivity changes are more affected.

A similar evaluation of sensitivity to measurement error was conducted for the long electrode case. For simulations of the finger-like anomaly, (400% increase in resistivity), we added different sets of uniformly distributed random noise. We used +/- 1% to reflect our in-field experience that long electrode surveys tend to have lower measurement error than point electrode surveys. For voxels with the smallest changes, we found that differences between the tomographs with different noise sets were as large as 2.5%. For voxels with the largest changes, the differences ranged from 1% to 2%.

## Results - Physical Models

Some of the key conclusions derived from the numerical simulations were evaluated using laboratory-scale physical models. We have focused on targets that are more resistive than background because information from the Maljamar pilot study suggested that the CO<sub>2</sub> flood created resistivity increases.

Physical models allow us to test our inversion techniques under controlled conditions, using known target geometry, contrast and location. Data from these models were processed using the same inversion techniques applied to the Maljamar numerical model. The physical model tests allow us to generate data that had realistic levels of measurement error. These data allow us to evaluate the effect(s) of numerical error caused by approximations in the forward solution. Physical models allow us to relate the results of numerical simulations and field surveys.

### Long electrodes vs. target position:

We concentrated most of our physical model work on long electrode scenarios because there is relatively little work to date documenting their sensitivity, resolution, and performance. Alternatively, there is ample evidence regarding the performance of point electrode tomographs (see references given in the introduction). Figure 12 presents some of the results obtained with the long electrode physical model. Details of the physical model are depicted in Figure 3. The tomographs indicate the resistivity change detected when a plastic pipe was inserted between the long electrodes. The plastic pipe creates resistivity increases intended as a model for a CO<sub>2</sub> flood. The top image row shows the changes when the pipe crosses the region of interest from end to end; the bottom row shows the results when the pipe extends half-way across.

The images in Figure 12 suggest that the resistivity changes are relatively small, typically showing changes that are less than 7%. This reduced sensitivity is due to the fact that long electrodes measurements integrate the electrical resistivities along their entire length. Consequently, resistivity changes caused by a pipe target with a diameter that is 4.5% of the total casing length are greatly reduced in magnitude. Similar reductions were observed in the Maljamar numerical model where changes between 10 and 15% were observed (see Figure 6, Maljamar numerical model results, resistivity increased 400%). A second similarity between the physical and numerical model results is that both suggest that long electrode tomographs provide useful information about the horizontal position, size, and shape of the region.

We also evaluated the effect that different measurement schedules have on the accuracy of the images. “Measurement schedule” is the sequence of transmitter and receiver dipoles used to measure the electrical properties of a region. The study indicated that it is important to use a “symmetric” schedule. By this we mean that the dipoles used should be evenly deployed relative to two vertical symmetry planes; these planes intersect at the center well and are parallel to the sides of the nine-spot pattern. Examples of symmetric and asymmetric schedules are presented in Figure 13. Schedule C in the figure is analogous to a conventional dipole-dipole schedule one would use for a linear array of electrodes (e.g. electrodes in a borehole), i.e., we have deformed the linear array by

bending it at the corners where electrodes 3, 5, 7, and 8 are located, and sampled numerically-adjacent dipoles. In contrast, schedule A shows a modified pole-pole schedule where one pole remains fixed while the other visits all other electrodes in the pattern. The fixed pole is then moved to the next electrode along the perimeter, and so on. Schedule B consists of a modified dipole-dipole schedule that consists of complimentary combinations of spoke and perimeter dipoles (as shown in the figure). In our study, we considered all three schedules shown as well as a random schedule (dipoles deployed in a random manner). It quickly became apparent that symmetric schedules produced better results. Thus, we have concentrated on symmetric schedules.

The tomographs in Figure 12 can be used to illustrate the effect of different schedules. Images corresponding to schedules A (left column) and B (right) are shown. We see that schedule B produces somewhat better results in that stronger changes are reconstructed. Both schedules result in images that approximately locate the plastic pipe.

We also performed numerical simulations of the physical model experiment; some of these results are shown in Figure 14. The first two columns of images compare the physical and numerical model results for schedule A. While the results are not exactly identical, they are similar. This suggests that numerical approximations made by the forward and inverse algorithms (e.g., the conductive vertical structures representing the long electrodes) are acceptable, resulting in fair reproductions of the experimental conditions.

The second and third column of images compare schedule A and schedule C results. The top images show significant differences: schedule A produces an anomaly that extends from side to side whereas schedule C produces an anomaly that seems to pinch out towards the left. We also investigated a randomized schedule where the transmitter and receiver dipoles were randomly located (results not included in the figure); this approach produced anomalies that least resembled the model target.

A second inversion approach that one may consider using is the “robust inversion” approach described by Morelli and LaBrecque, 1996. According to the authors, this approach is well suited when the data variances are not known, or when there are outliers in variance. Their approach modifies the weights contained in the matrix  $\underline{W}$  (see equation 4 in an earlier section). We evaluated this approach using our physical model data and compared the results with and without the technique. The comparisons suggest that when the re-weighting technique is used, weaker anomalies are produced. We suggest the following reason for this. The inversion algorithm determines how closely each reading fits a given resistivity model. When some readings differ greatly from the majority, they are given a lesser weight because it is assumed that the larger differences are caused by measurement error. While the re-weighting technique can enhance the quality of the inversions in cases with abundant data (e.g., point electrode surveys), it may be counter-productive in the case of long electrode surveys with sparse data where a few measurements may exhibit a high sensitivity to the anomalous region. Thus, for long electrode surveys, a constant data weighting produces more realistic anomaly magnitudes as long as data quality is accurate.



### Point electrodes:

Our physical modeling study also considered point electrode scenarios. The electrode layout used is depicted in Figure 3. This model represents a “four-spot” pattern that is roughly equivalent to one quadrant in the “nine spot” pattern assumed for the Maljamar numerical model. The primary purpose for this phase of the work is to evaluate the capacity to estimate target volume using point electrode tomographs and various resistive targets. For each material type, we constructed four targets of increasing volume by using between one and four blocks grouped together.

Some of the images produced for this physical model are presented in Figure 15. The top row of images shows the target location and changing volume as additional blocks are grouped together. The bottom row of images shows the reconstructed resistivity change caused by foam blocks with the highest porosity; this material offered the smallest resistivity contrast of all materials considered (36%); other contrasts considered were 200% and  $10^8$  %. The white bar over the color bar indicates the range of values that have been rendered transparent. The tomographs show zones of resistivity change in approximately the correct locations. As the volume of the target increases, the anomaly size grows larger and shows larger resistivity changes. The reconstructed size of the anomaly is substantially larger than the true target size. The exaggerated size is a direct consequence of the smoothness-constrained, objective function used by the inversion algorithm. Other regularization approaches can be considered such as minimizing differences relative to an a-priori model (e.g. Mackie et al, 1988). Consideration of alternate regularization schemes was outside our scope of work, and we leave it to other investigators to evaluate them.

We now compare the size of the reconstructed anomalies to the size of the physical model. The results are shown by the top row of plots in Figure 16. The plot on the left displays volume ratio (observed volume divided by true volume) as a function of model resistivity change. For this analysis, we summed up the volume of all voxels that displayed a change in resistivity equal to or larger than 10%; changes below that level were arbitrarily assumed to be unreliable due to measurement error. The numbers 1 through 4 on the plot legend refer to the number of blocks included in the target (e.g. the number three indicates that 3 blocks of equal volume were combined and the target volume is three times as large as for the case labeled with a one). The plot shows that in all cases, the volume is overestimated (all volumes ratios are greater than 1.0). The volume estimates generally improve (get closer to 1.0) as the target volume increases. Volume ratios increase when the contrast changes from 36 to 220% (foam targets), and slightly decrease for the  $4.0\text{E}+08$  case (plastic targets). The increases are consistent with the trends observed in the Maljamar numerical model, and we believe are due to smooth models produced by the inversion algorithm. The slight decrease for the  $4.0\text{E}+08$  case is not currently understood. Perhaps the high contrast produced by the plastic target results in data with a higher signal to noise ratio. The purpose of the smoothness constraint is to stabilize the inversion. During inversion, higher quality data may require a lower level of smoothing thereby resulting in tomographs that are closer to the truth.

We now compare the numerical and physical results in Figure 16. The right plot shows the results for data generated numerically to simulate the physical model surveys. They show approximately similar trends in that observed volumes get closer to the truth as the magnitude of resistivity change gets smaller. Also, except for two points, both plots suggest that volume ratios get closer to 1.0 as the volume of the target increases. A clear difference between the plots is that the physical model reconstructions over-predict volume to a higher degree than the numerical simulations. We suggest that modeling error may be the cause of this difference. The physical model data were acquired in a continuous system but was modeled using a discretized, piece-wise constant domain. Modeling error arises from this and other approximations, thereby increasing the level of “noise” affecting the physical model inversions.

The bottom plot shows the volume ratios calculated for the Maljamar numerical study. Comparing all three plots in Figure 16 leads us to some interesting conclusions. We realize that comparing scenarios of vastly different scales can be problematic, but our intent here is to look for similar trends (if any) in order to gain confidence in the predictions based on the Maljamar study. Consistent trends among the three plots are: 1) reconstructed volumes are typically larger than target volume, 2) reconstructed volumes move closer to the truth as target volume increases, and as the magnitude of resistivity change decreases. We suggest that the similarity in trends between these cases give us confidence in the conclusions reached for the Maljamar study.

## CO<sub>2</sub> Volume Estimates

The ERT method provides three-dimensional tomographs of the reservoir volume that has experienced a change in resistivity. This volume is not the volume of the CO<sub>2</sub> in the reservoir but rather the volume of reservoir rock affected by the CO<sub>2</sub> flood. As indicated earlier, to estimate the volume of rock invaded by the CO<sub>2</sub> flood, one simply sums the volume of all voxels that exhibit a level of change that is determined to be credible. However, reservoir managers will not be interested in the plume volume; they will want to know the CO<sub>2</sub> fluid volume trapped within this region. Estimates of fluid volume can be made by using the 3D tomographs together with a petrophysical model relating resistivity to rock moisture content to estimate released volume.

The petrophysical model we chose is widely accepted and is known as Archie’s equation (Hearst *et al.*, 2000). This model relates the rock’s resistivity ( $\rho_r$ ) to the water saturation ( $S_w$ ), porosity ( $\phi$ ), and pore water conductivity ( $\rho_w$ ) as follows:

$$\frac{\rho_r}{\rho_w \phi^{-m}} = S_w^{-n} \quad (5)$$

The exponents  $m$  and  $n$  are empirically derived constants. We assume that the electrical resistivity of CO<sub>2</sub> is very high so that it is electrically equivalent to air, that CO<sub>2</sub> does not dissolve in the oil phase, and that it does not react with the rock/water system; the validity of these assumptions is not known. We also assume that only water and CO<sub>2</sub> fill the pore space. Given these assumptions, we can derive the following equation:

$$\frac{S_{w,a}^{-n}}{S_{w,b}^{-n}} = \frac{\rho_{wb}}{\rho_{wa}} \frac{\rho_{ra}}{\rho_{rb}} \quad (6)$$

Note that the assumption that CO<sub>2</sub> does not react with the rock/water system implies that  $\frac{\rho_{wb}}{\rho_{wa}} = 1.0$ . The subscripts *b* and *a* indicate conditions before and after the rock's property change due to CO<sub>2</sub> invasion. Hearst *et al.* indicate that the exponent *n* is generally determined based on laboratory data and when such data are unavailable, an acceptable value is about 2.0 +/- 0.5. Once the change  $\frac{S_{w,a}}{S_{w,b}}$  is established, the change in pore water volume can be calculated as follows:

$$V_w = \left( \frac{S_{w,a}}{S_{w,b}} - 1 \right) S_{w,b} \phi V_v \quad (7)$$

where  $V_w$  is the change in the volume of water in each voxel and  $V_v$  is the volume of the voxel. In most cases, good estimates of  $S_{w,b}$  and  $\phi$  can be obtained from geophysical well logs and /or laboratory measurements made on core. If we assume that the pore volume is filled with only water and/or CO<sub>2</sub>, then:

$$V_{CO_2} = \phi V_v - V_w \quad (8)$$

We used equation 8 to estimate  $V_{CO_2}$ , the change in CO<sub>2</sub> volume on a voxel by voxel basis. We then summed all voxel estimates to obtain total volumes for the “model” and reconstructed targets. The following assumptions were made:  $S_{w,b}$ , equals 1.0, the exponent *n* equals 2 for both “before” and “after” saturation, and  $\phi$  equals 0.3.

#### Maljamar numerical study – point electrodes:

Figure 17 shows the volume estimates for the Maljamar numerical model targets. The tomograph-derived estimates have been normalized to the true volumes for each target. The figure shows normalized volume (i.e., volume ratios) as a function of resistivity change, and as function of target (L1-L6 identified in Figure 3). One trend in the figure is that the volume ratios generally get closer to 1 as the resistivity contrast increases. For 10% change, there is a steep rise in the normalized volumes. We believe that the relatively large increases exhibited by the 10% anomalies is caused by two related issues: A) Smaller changes in resistivity are associated with smaller CO<sub>2</sub> volumes (see equations 6 – 8). This means that to compute the normalized volume, we are dividing by a much smaller volume for the 10% anomalies, thereby creating some of the non-linear behavior in Figure 17, and B) the anomalies produced by the smaller changes in resistivity are most affected by degraded signal to noise ratio. Evidence for this was already shown in Figure 11. As these erroneous changes are relatively large, the volume estimates become

increasingly unreliable. These plots suggest that field procedures that improve data signal to noise ratios result in better CO<sub>2</sub> volume estimates.

We now return our attention to Figure 17. A second trend in the figure is that volume ratios get smaller as the true volume increases. For all contrasts (excepting –80%), target L3 (finger-like anomaly) has the smallest volume and exhibits the largest normalized volumes. Alternatively, targets L4 and L5 have the largest volumes and exhibit the smallest normalized volumes. This means that the volume estimates become more accurate as the volume of the anomaly gets larger. We believe that this another manifestation of the signal to noise problem discussed above. All other conditions being equal, larger anomalies produce larger changes in measured resistance; the larger changes become easier to detect when measurement noise is present.

Note that when a target creates resistivity increases (positive percent change in contrast), the normalized volume is above 1.0. For targets creating a resistivity decrease (negative percent change), the normalized volume is less than one (values displayed in Table 1 below). While the decreasing resistivity scenario is not relevant for CO<sub>2</sub> sequestration, we considered it for volume estimation so that we could compare the volume estimates of conductive and resistive targets. Table 1 suggests that volumes for resistive targets will be over-predicted while volumes for conductive targets will be under-predicted. For example, targets that increased resistivity five-fold (400% contrast), exhibit normalized ratios ranging from 2.2 to 4.5. For CO<sub>2</sub> targets similar to those assumed for the Maljamar numerical model, we would expect that volume estimates based on ERT tomographs would over-predict the volume somewhere in this range.

Binley et al., 2002 report field results that are consistent with our predictions for conductive anomalies. Their data suggest that ERT images of conductive plumes under-predicted their true volume by approximately 50%.

Targets that changed resistivity five-fold (–80% and +400% contrast), exhibit the normalized ratios listed below:

Model	–80 %	+400%
L1	0.22	3.1
L2	0.92	3.4
L3	0.00	4.2
L4	0.69	2.2
L5	0.92	2.4
L6	0.73	3.2

Table 1 shows the normalized ratios for the –80% (five fold decrease) and +400% anomalies (five fold increase).

For resistivity change of -80%, the largest volume targets (L2, L4, L5, and L6) produced normalized volumes ranging from 0.69 to 0.92; the lower volume targets (L1, L3) did substantially poorer. Volume estimates for the larger volume targets are more accurate (closer to a normalized volume equal to 1) than those for the resistive targets of the same volume. For example, target L5 produces normalized volumes of 2.4 (resistive target) and 0.92 (conductive target). Similarly, target L4 produces normalized volumes of 2.2 (resistive target) and 0.69 (conductive target). We do not know exactly why the larger conductive targets are more accurate than the larger resistive targets. We speculate that when targets are conductive, more current can flow within its interior, thereby increasing sensitivity, and leading to tomographs that more accurately represent the target's interior resistivities.

#### Water tank physical models – point electrodes:

We used tomographs of physical models to evaluate the volume estimation trends predicted on the basis of numerical models in the previous section. Two types of foam were used to fabricate targets (porosities of 0.56 and 0.85) that were immersed in a water tank. We used equations 7 and 8 to calculate the volume of the foam solid phase (resistive) in the porous targets. The solid phase is electrically analogous to the CO<sub>2</sub> fluid within a porous reservoir.

We recognize that there are significant differences in scaling, number of electrodes, aspect ratio, etc. between the physical and numerical models. Our goal is to observe qualitative trends in the volume estimates for the numerical models and to compare these to the numerical model trends. If they are similar, we gain confidence that the volume estimate trends for the Maljamar model are likely to be reasonable.

Figure 18 shows volume ratios for the foam targets. The curve for the highest porosity foam shows that volume ratio decreases as true volume increases. Three out of the four points for the lowest porosity foam show a similar trend. Also, the foam target curves suggest that for resistive targets, the volumes are over-predicted by a factor ranging from about 2 to about 4.3. Both of these trends are qualitatively similar to those observed for resistive targets in the Maljamar model.

## **Summary and Conclusions**

The results of the numerical and physical modeling study described here increase our confidence that the ERT method can provide useful information to operators and managers controlling CO<sub>2</sub> field operations regarding the progress and behavior of the CO<sub>2</sub> flood. In practice, ERT surveys would be conducted to produce time dependent maps of changes in formation resistivity caused by CO<sub>2</sub> injection and migration. ERT tomographs may be used to identify reservoir locations accepting CO<sub>2</sub>, lateral extent of the flood, fluid flowpaths, and coarse estimates of the CO<sub>2</sub> volume retained in the reservoir

This study quantifies the effects of a variety of factors that affect the resolution and fidelity of the ERT method, under realistic conditions of scale, contrast and measurement error. Information such as the shape, location, and lateral extent of the flood can be deduced. If point electrode arrays or horizontal wells are available, information regarding the vertical extent may also be deduced. Results from physical models suggest that several of the trends observed in the numerical study are reasonable and likely to be valid.

- 1) Of the electrode deployment scenarios considered, the “point” electrode approach offers the highest sensitivity to the changes caused by the CO<sub>2</sub> flood. This approach requires observation wells that contain electrodes. For even the most challenging anomaly shape considered, and typical measurement errors (approximately 2%), anomalies that cause resistivity changes on the order of 30% or larger can be detected and resolved reliably. When unusually low measurement errors (0.2%) are possible, resistivity changes as low as 10% can be reliably detected and resolved.
- 2) Vertical and horizontal steel casings can be used together as long electrodes to coarsely resolve vertically and horizontally the changes caused by a CO<sub>2</sub> flood. This approach does not require observation wells. When only vertical steel casings are used as long electrodes, the shape of the anomaly can be resolved laterally but not vertically. Results from physical models confirm that long electrode tomographs can be used to infer approximate target shape and lateral position. These results suggest that it may be possible to map changes associated with a CO<sub>2</sub> flood using long electrodes. This approach helps reduce costs by reducing or eliminating the need for dedicated observation wells, and by minimizing disruption to reservoir operations in order to make measurements using injector/producer wells.
- 3) The tomographs tend to exaggerate the size of the anomalies and under-predict the magnitude of the changes in resistivity. These effects are largely independent of measurement error and probably dependent on the regularization approach (models with maximum smoothness) used by the inverse algorithm. The regularization used tends to “smear” the resistivity values from any given voxel to adjacent voxels, thereby exaggerating the volume and under-predicting the resistivity. Tomographs of physical models confirm the following trends for resistive targets: a) interpreted volumes are typically larger than actual volumes and observed resistivity changes are lower than model resistivity change, b) observed volumes get closer to the truth as target volume increases, and as the magnitude of resistivity change decreases. We suggest that the similarity in trends between the numerical and physical model studies indicates that conclusions reached for the Maljamar study are likely to be reasonably close to reality.
- 4) Estimates can be made of CO<sub>2</sub> volume that remains trapped within the reservoir. The accuracy of these estimates is strongly dependent on factors listed under item 3. Volumes for resistive fluids are likely to be over predicted while values for conductive anomalies will probably be under-predicted. When CO<sub>2</sub> floods cause resistivity increases similar to those observed during the Maljamar pilot study (400%), the numerical models suggest that their volume will be overestimated by a factor of 3-4. Physical model studies suggest that volume will be over-predicted for resistive targets by a factor of 2-4.

- 5) The easiest anomalies to resolve are those located near the center of the 9 spot pattern considered, and those having the largest volume and contrast. The most difficult anomalies to resolve are “finger” anomalies of low volume and contrast.
- 6) CO<sub>2</sub> breaches of the caprock may be hard to resolve for typical oil field well separations. These breaches may be coarsely resolved when the breach occurs close to a “point” electrode array.

## **Acknowledgements**

We gratefully acknowledge the support of DOE’s Office of Basic Energy Sciences. Dr. Andrew Binley (Lancaster University, Lancaster, England) suggested ideas that improved our analysis of volume estimates and provided many helpful comments as an informal reviewer of this work. Drs. W. Frangos and G. Morelli served as formal reviewers and similarly provided many helpful comments. Drs. William Hanley and Ronald Glaser (LLNL) provided guidance regarding the statistical analysis of noisy data. This work was performed under the auspices of the U.S. Department of Energy by University of California Lawrence Livermore National Laboratory under contract No. W-7405-Eng-48.

## **References**

- Albright, J. C., 1984. Use of well logs to characterize fluid flow in the Maljamar CO<sub>2</sub> Pilot, Society of Petroleum Engineers (SPE) 59<sup>th</sup> Annual Technical Conference and Exhibition, Houston Texas, September 16-19, *SPE 1342*, 8 pp.
- Binley, A., S. Henry-Poulter and B. Shaw, 1996, Examination of solute transport in an undisturbed soil column using electrical resistance tomography, *Water Resour. Res.*, **32**(4), 763-769.
- Binley, A., P. Winship, M. Pokar and J. West, 2001, Cross-borehole radar and resistivity tomography: A comparison of techniques in unsaturated sandstone, In: Proc. Symp. Applications of Geophysics to Engineering and Environmental Problems (SAGEEP2001), Environmental and Engineering Geophysical Society, Denver, CO.
- Binley, A., G. Cassiani, R. Middleton, and P. Winship, 2002, Vadose zone model parameterisation using cross-borehole radar and resistivity imaging, *Journal of Hydrology*, vol. 267, pp 147-159.
- Daily, W., A. Ramirez, D. LaBrecque and J. Nitao, 1992. Electrical Resistivity Tomography of Vadose Water Movement, *Water Resources Research*, v. 28, no. 5, 1429-1442.
- Daily, W. D., A. Ramirez and R. Johnson, 1998, Electrical impedance tomography of a perchloroethylene release, *J. Envir. and Eng. Geophysics*, vol. 2, No. 3, pp. 189-201.
- Daily, W. and A. Ramirez, 2000, Electrical imaging of engineered hydraulic barriers, *Geophysics*, vol. 65, no. 1, pp. 83-94.

Hearst, J., P. Nelson, and F. Paillett, 2000, *Well Logging for Physical Properties*, John Wiley and Sons NY, NY.

Kemna, A., A. Binley, A. Ramirez, and W. Daily, 2000, Complex resistivity tomography for environmental applications, *Chemical Engineering Journal*, vol. 77, p. 11-18.

LaBrecque, D. J., M. Miletto, W. Daily, A. Ramirez, and E. Owen, 1996, The effects of Noise on Occam's Inversion of Resistivity Tomography Data, *Geophysics*, vol. 61, no. 2, pp. 538-548.

LaBrecque, D., G. Morelli, W. Daily, A. Ramirez, and P. Lundegard, 1999, Occam's inversion of 3D Electrical Resistivity Tomography, in "Three-dimensional electromagnetics", eds. M. Oristaglio, B. Spies, and M.R. Cooper, Soc. Of Exploration Geophysicists, pages 575-590.

Lundegard, P. D. and LaBrecque, D. J., 1995, Air sparging in a sandy aquifer (Florence Oregon): actual and apparent radius of influence, *Journal of Contaminant Hydrology*, **19**, 1-27.

Mackie, R., B. Bennett, and T. Madden., 1988, Long-period magneto-telluric measurements near the Central California coast: a land-locked view of the conductivity structure under the Pacific Ocean, *Geophys. J.*, **95**, 181-194.

Morelli, G., and D. LaBrecque, , 1996, Robust scheme for ERT inverse modeling, Symposium on the Application of Geophysics to Engineering and Environmental Problems (SAGEEP) '96, Keystone, CO., April 28 – May 2, 1996, 629-638.

Newmark, R.L., W.D. Daily, K.R. Kyle and A. L. Ramirez, 1998. Monitoring DNAPL pumping using integrated geophysical techniques, *Journal of Environmental and Engineering Geophysics*, v. 3, no.1, 7-14.

Newmark, R.L., W. Daily, A. Ramirez, 1999. Electrical resistance tomography using steel cased boreholes as electrodes (UCRL-JC-131572), Society of Exploration Geophysicists 1999 SEG Annual Meeting, November, 1999.

Newmark, R.L., W. Daily, A. Ramirez, 2000. Electrically imaging EOR stimulation using steel-cased boreholes, (SPE 62567), SPE/AAPG Western Regional Meeting, June 19-23, Long Beach, California.

Oldenburg, D.W. and Y. Li, 1994, Inversion of induced polarization data, *Geophysics*, **59**, 1327-1341.

Ramirez, A., W. Daily, A. Binley, D. LaBrecque, and D. Roelant, 1996, Detection of leaks in underground storage tanks using electrical resistance methods, *Journal of Environmental and Engineering Geophysics*, Vol. 1, no. 3, 189-203.



- Ramirez, A., W. Daily, D. LaBrecque, E. Owen and D. Chesnut, 1993, Monitoring an Underground Steam Injection Process Using Electrical resistance Tomography, *Water Resources Research*, vol. 29, no. 1, pp 73-87.
- Ramirez, A. and W. Daily, 2001, Electrical imaging of the large block test – Yucca Mountain, Nevada, *Journal of Applied Geophysics*, vol. 46, p. 85-100.
- Sasaki, Y., 1994, 3-D resistivity inversion using the finite-element method, *Geophysics*, **59**(11), 1839-1848.
- Schima, S., LaBrecque, D. J, and Lundegard, P. D., 1996, Using resistivity tomography to monitor air sparging, *Ground Water Monitoring and Remediation*, **16**, 131-138.
- Shi, W., W. Rodi, M. Toksoz, and D. Morgan, 1997. Three dimensional electrical resistivity tomography and its application to Larderello-Valle Secolo geothermal field in Tuscany, Italy, Symposium on the Application of Geophysics to Engineering and Environmental Problems (SAGEEP) '97, Reno, NV., March 23 – 26, 1997, Vol. II, 889-899.
- Slater, L., Zaidman, M.D., Binley, A.M. and West, L.J., 1997a, Electrical imaging of saline tracer migration for the investigation of unsaturated zone transport mechanisms, *Hydrology and Earth System Sciences*, **1**, 291-302.
- Slater, L., A. Binley, D. Brown, 1997b, Electrical Imaging of the Response of Fractures to Ground Water Salinity Change, *Ground Water*, **35**(3), 436-442.
- Tikhonov, A. N. and Arsenin, V. Y., 1977, Solutions of ill-posed problems, ed. Fritz, J., John Wiley & Sonss, New York.

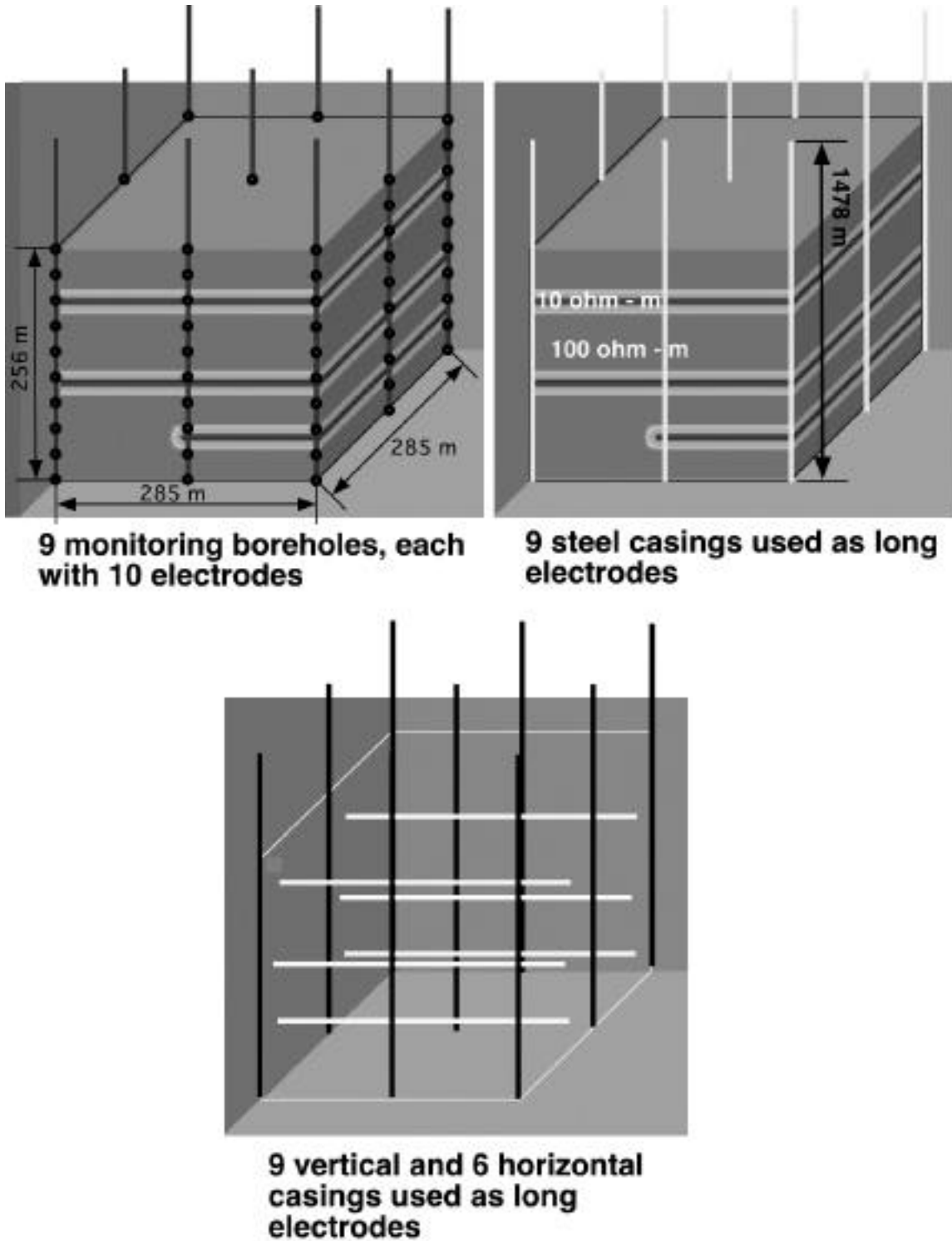


Figure 1 shows the electrode configurations considered for the numerical study. All the configurations assume a 9 spot pattern and spatial scales typical of oil reservoirs. The study evaluated vertical arrays of point electrodes and metallic casings used as long electrodes.

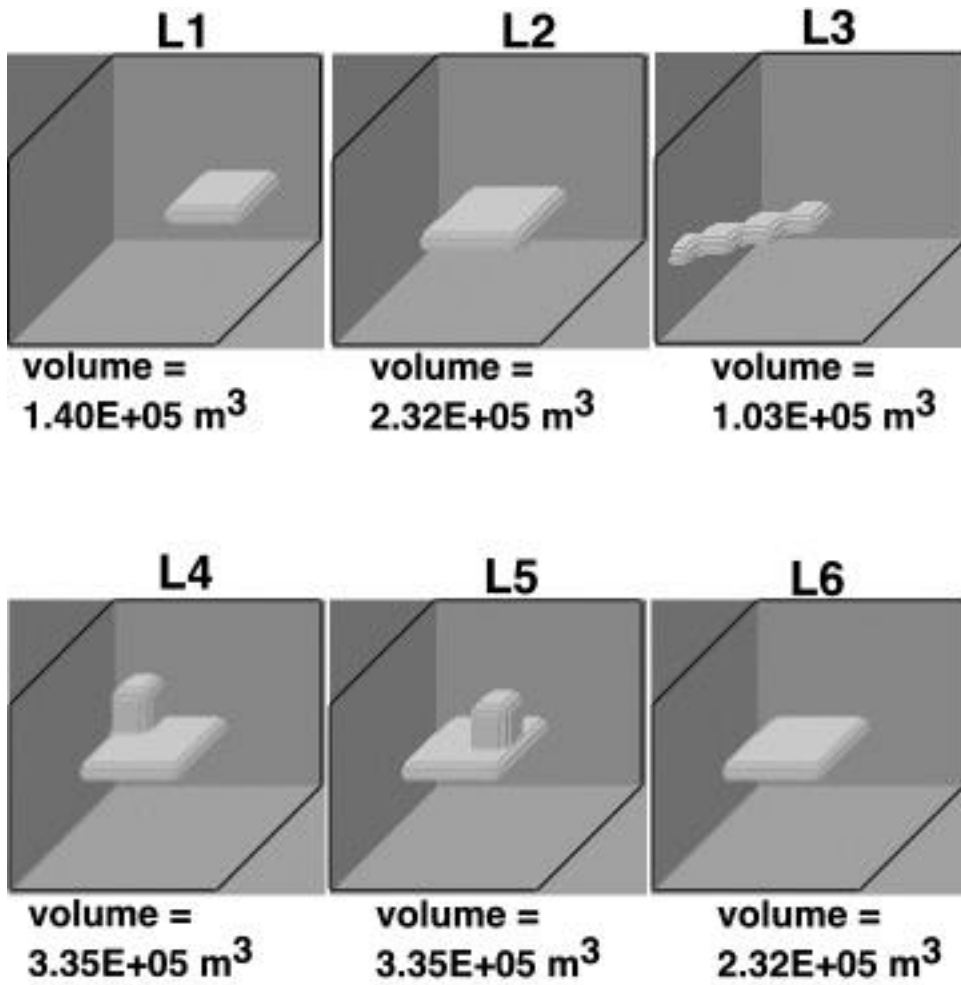


Figure 2 shows the targets used for the Maljamar numerical study. The target outline indicates the reservoir regions undergoing resistivity change due to a simulated CO<sub>2</sub> flood. We considered tabular anomalies, a “finger” anomaly (L3) and anomalies that penetrated the caprock above the reservoir (L4 and L5).

**Physical model simulating  
four point electrode arrays  
(one quadrant of a nine spot  
pattern)**

**Physical model simulating  
steel casings in a nine spot  
pattern**

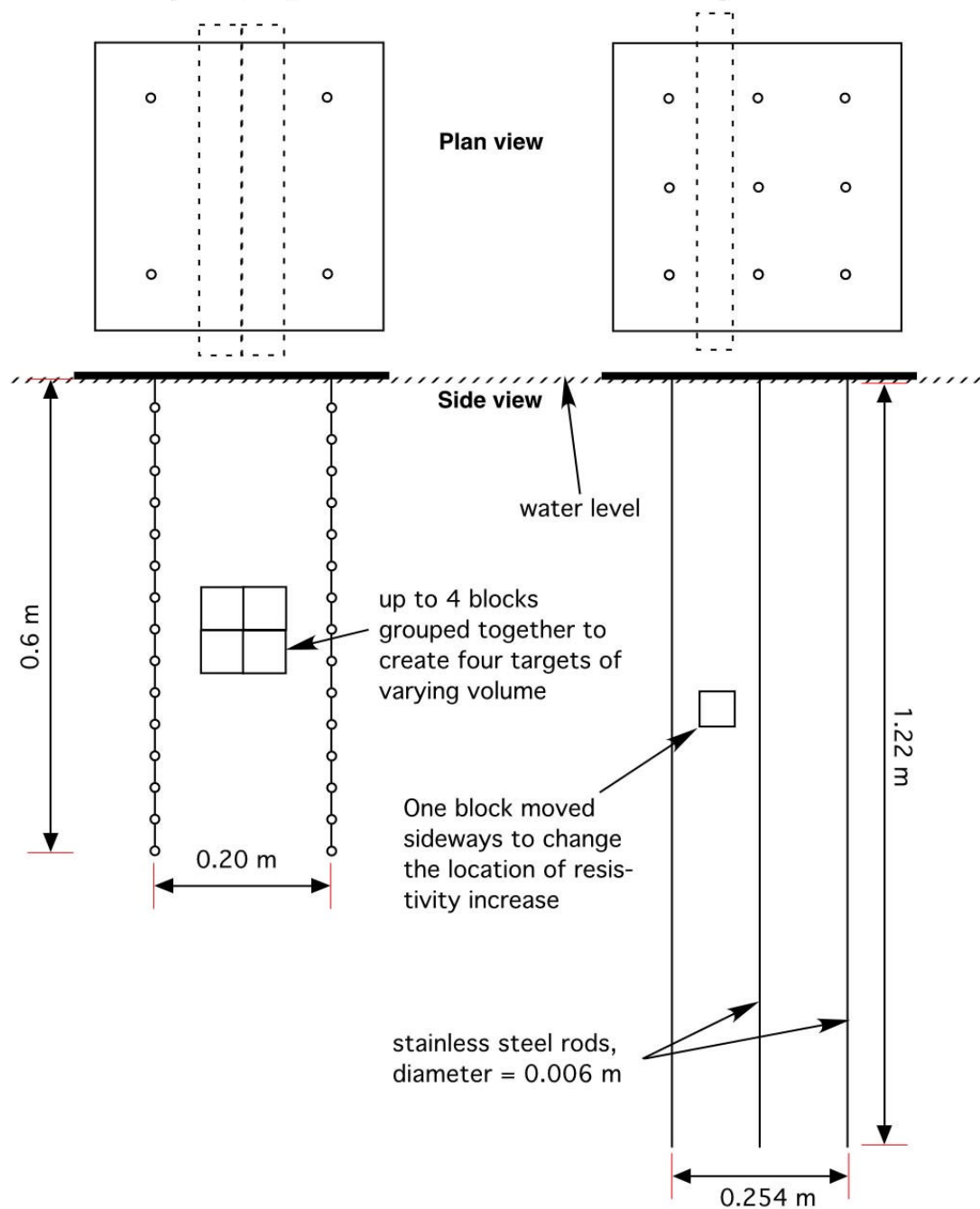


Figure 3 shows the electrode layouts used for the physical model study. One model made use of vertical point electrode arrays (drawings on the left) and a second model used long electrodes (drawings on the right).

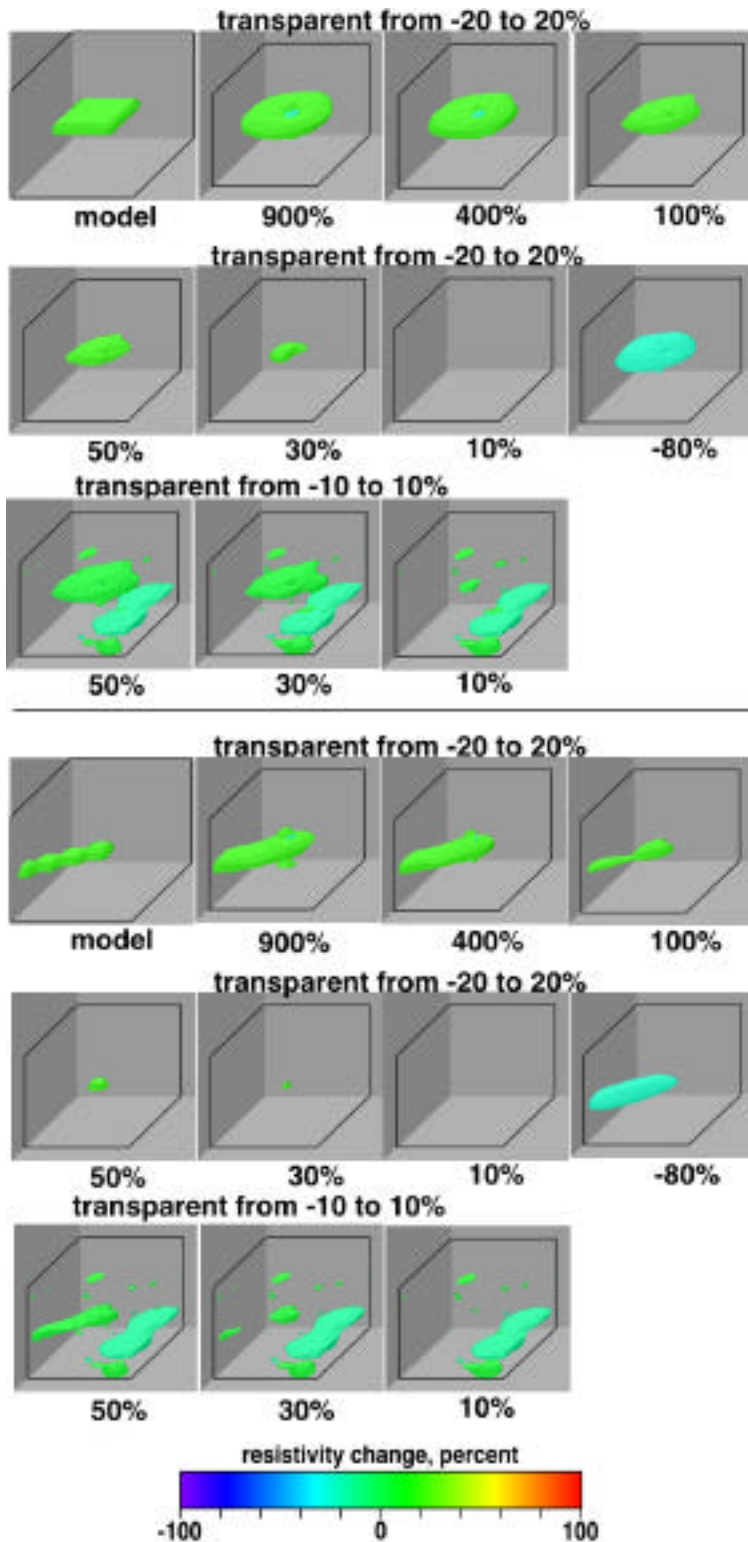
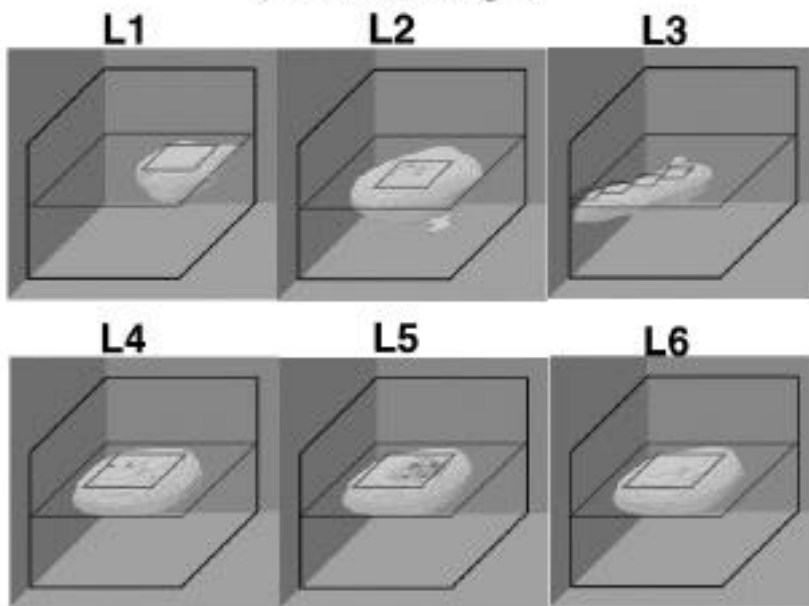


Figure 4 shows point electrode results for two target models. The top three rows of images show the resistivity changes reconstructed for a tabular anomaly. The resistivity changes assumed ranged from +900% to -80%. The third row of images uses a smaller transparency range than the first two rows. The bottom three rows show the resistivity changes reconstructed for a "finger" anomaly.

**Target resistivity 5 times higher than baseline  
(400% change)**



---

**Target resistivity 5 times lower than baseline  
(-80% change)**

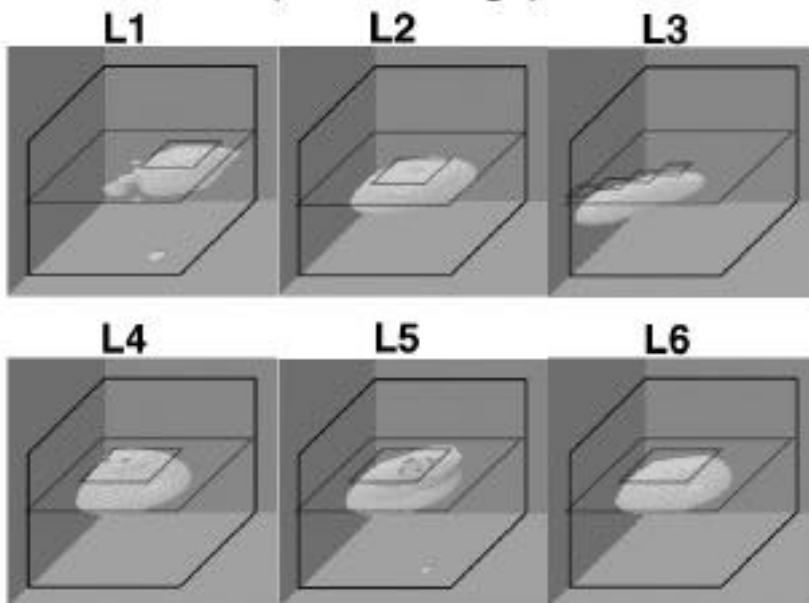
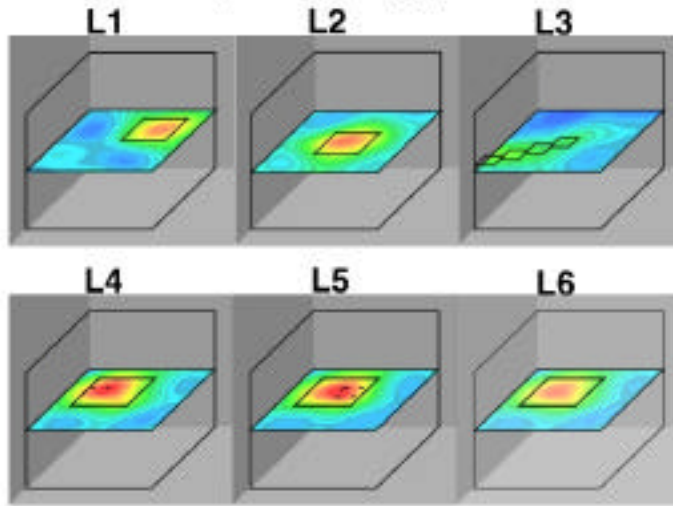


Figure 5 shows the point electrode results for all six targets. All targets either increased the pre-flood resistivity by a factor of 5 (+400 %) or decreased by a factor of 5 (-80%). The outline for the true model is superimposed on the tomographs. Transparent values lie in the range of +/- 20%.

**Target resistivity 5 times higher than baseline  
(400% change)**



**Target resistivity 5 times lower than baseline  
(-80% change)**

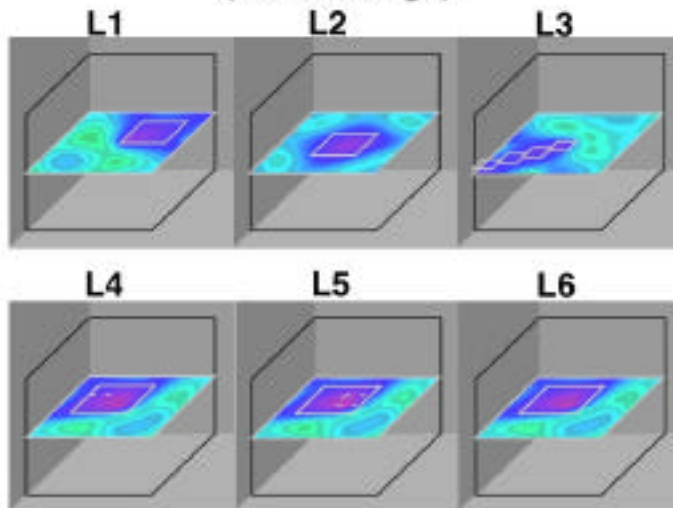
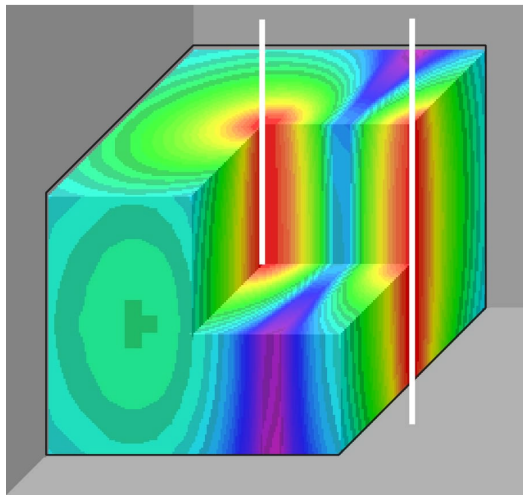


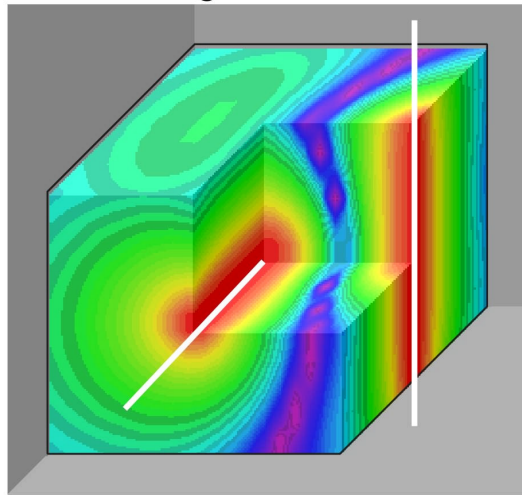
Figure 6 shows the long electrode results for all six targets. All targets increased the pre-flood resistivity by a factor of 5 (+400 %) or decreased by a factor of 5 (-80%). The outline for the true model is superimposed on the tomographs. These results can be compared with the point electrode results in Figure 5.

Two vertical steel casings



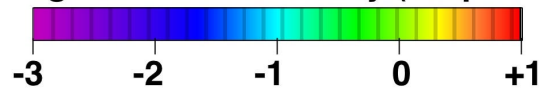
current in the formation flows horizontally

One vertical and one horizontal steel casings



current flows vertically and horizontally

log10 - current density (Amp/m<sup>2</sup>)



assuming 2 Ampere input

Figure 7 shows the distribution of current density for two scenarios. Left image: two vertical long electrodes form the transmitter dipole. Right image: a vertical and a horizontal long electrode form the transmitter dipole.



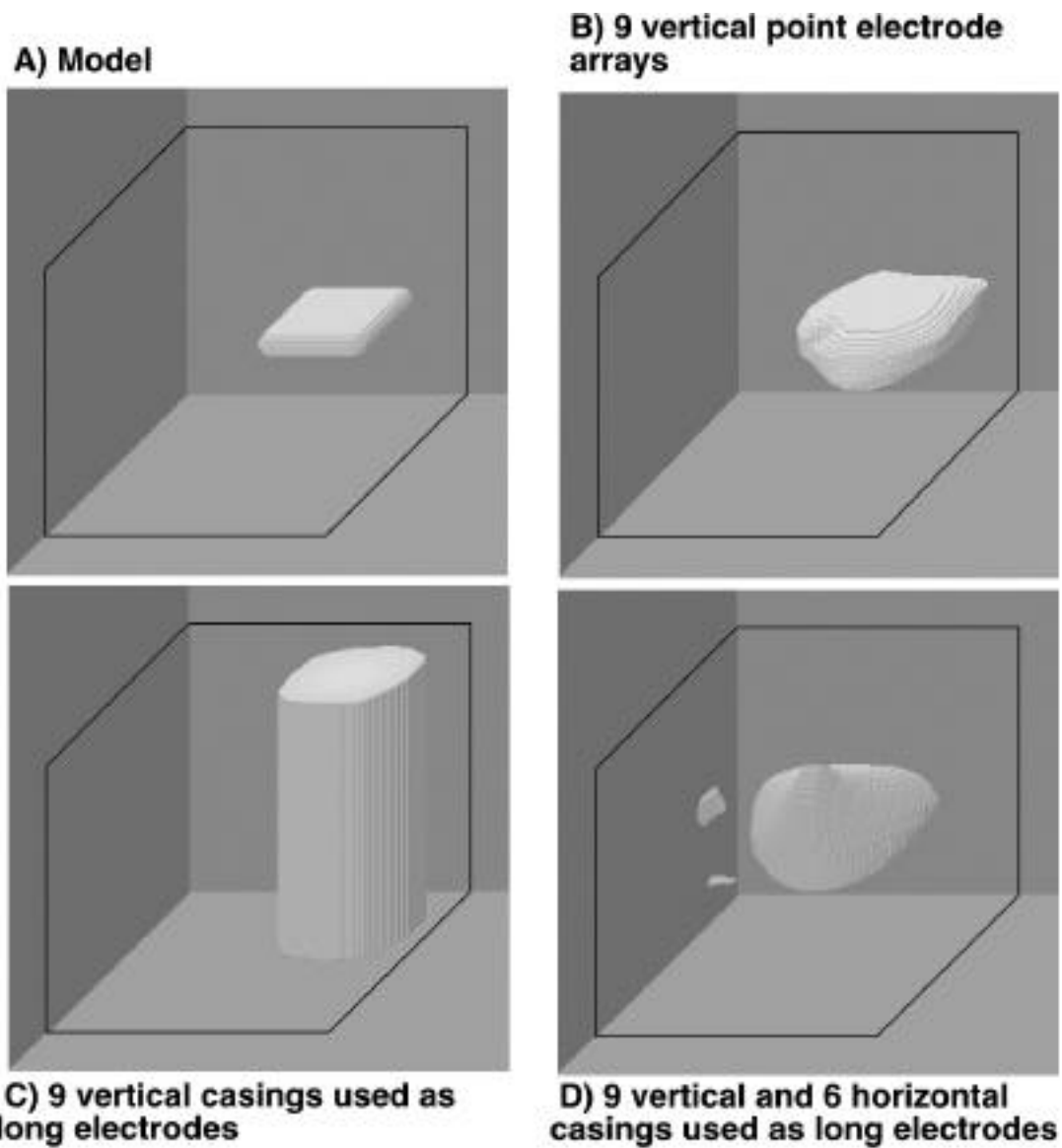


Figure 8 compares the tomographs obtained for the three electrode scenarios considered. In this case, we compare the results for the L1 model when the center layer resistivity changes from 10 to 50 ohm-m. For frames A and B, the transparent values lie in the range of  $\pm 20\%$ . For frames C and D, the transparent values lie in the range of  $\pm 5\%$ .

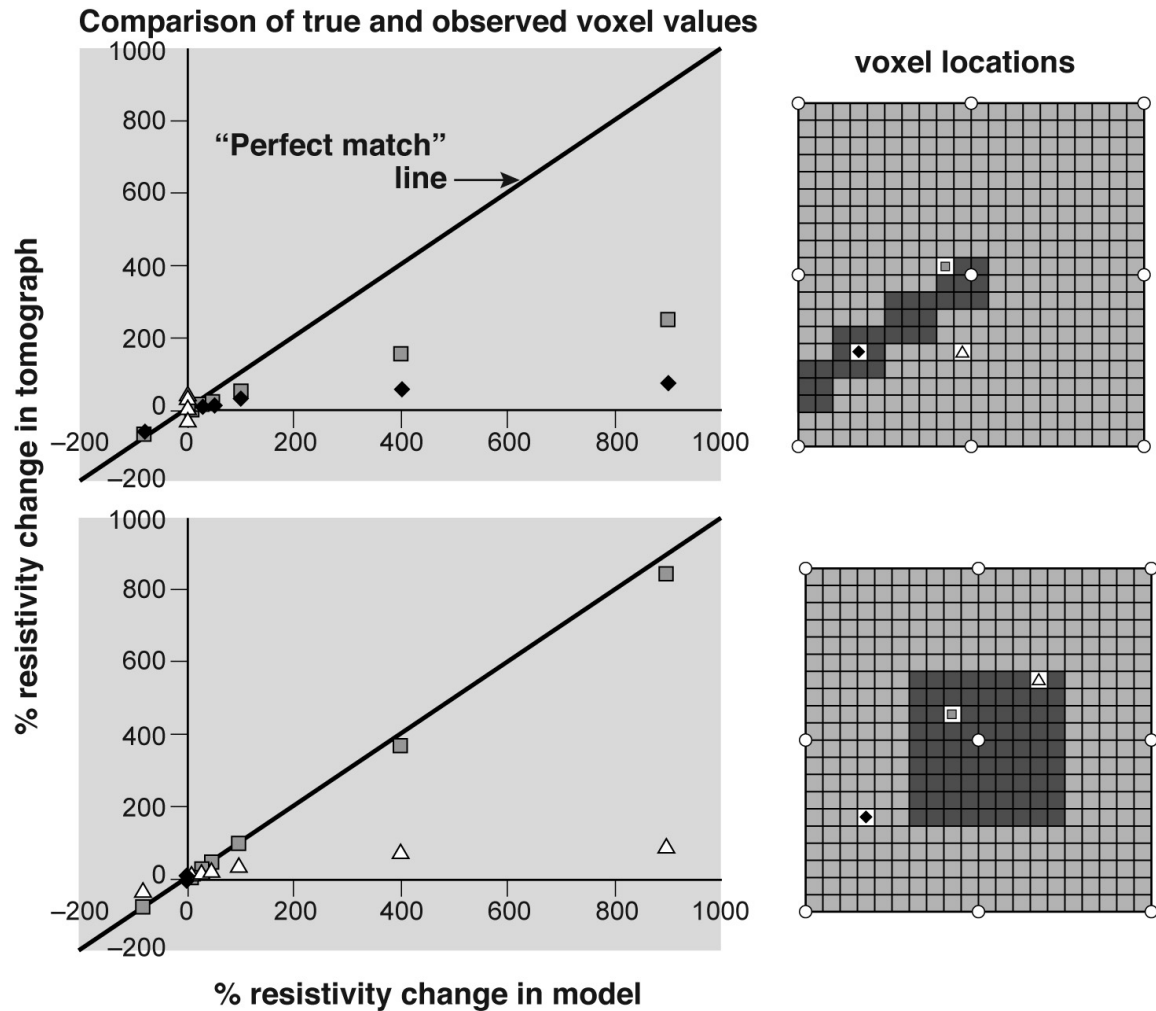


Figure 9 shows the influence of voxel position on the magnitude of the reconstructed resistivity changes. The graphs on the left side of Figure 9 compare the "true" percent resistivity change (in the model) to the recovered percent resistivity change in the tomograph for the various magnitudes of resistivity change considered. Horizontal slices through the 3D mesh are shown on the right hand side of the figure. These slices show the location of the anomalies in the mesh (dark gray areas), the location of the point electrode arrays (white circles), and the location of the voxels to be examined in the graphs.

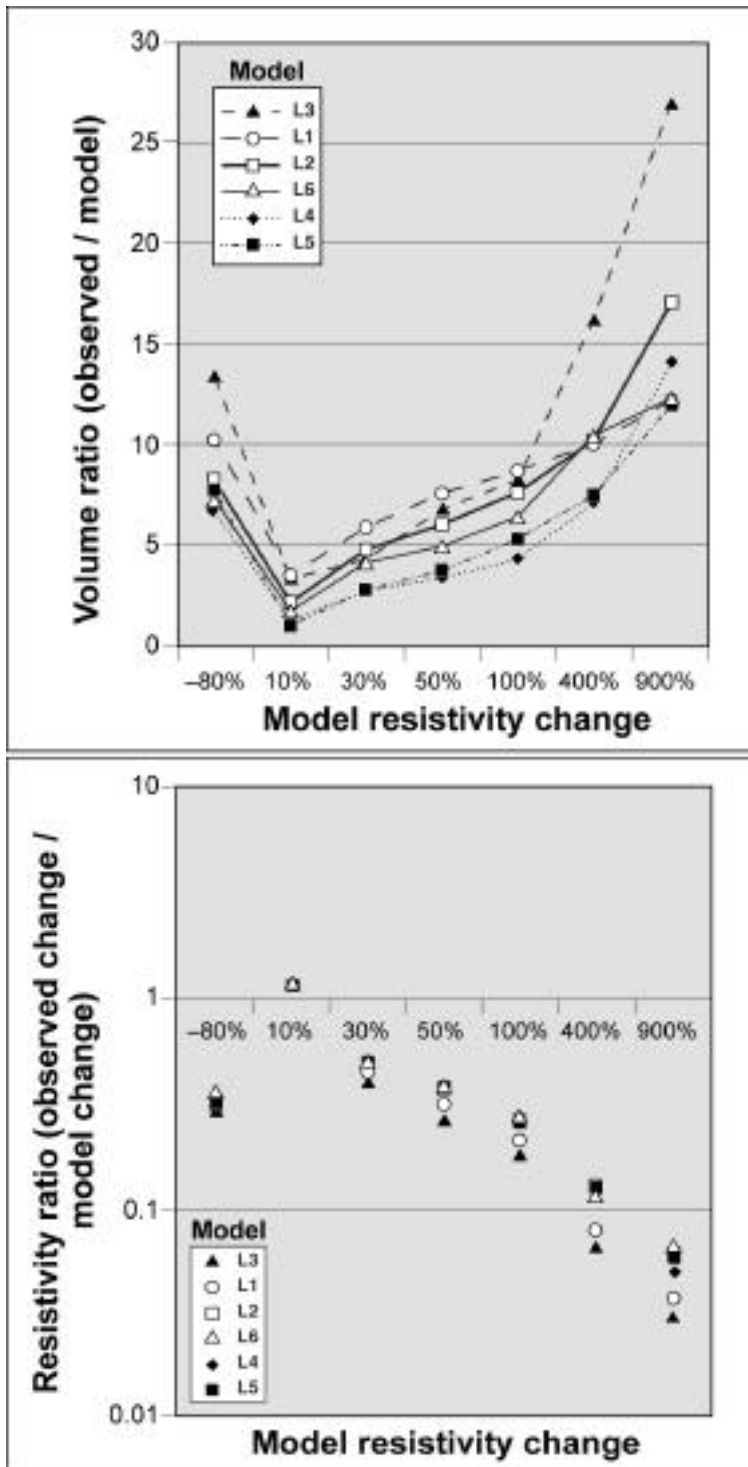


Figure 10. Comparison of the volume and average resistivity of the anomaly revealed by the tomographs and corresponding model values. The top graph shows the volume ratios obtained as a function of anomaly contrast and as function of model. The bottom compares the average tomograph resistivity of the voxels within the anomaly volume to the corresponding voxel resistivity values in the model. Note that the independent variable axis for both graphs, and the dependent variable axis for the bottom graph are non-linear.

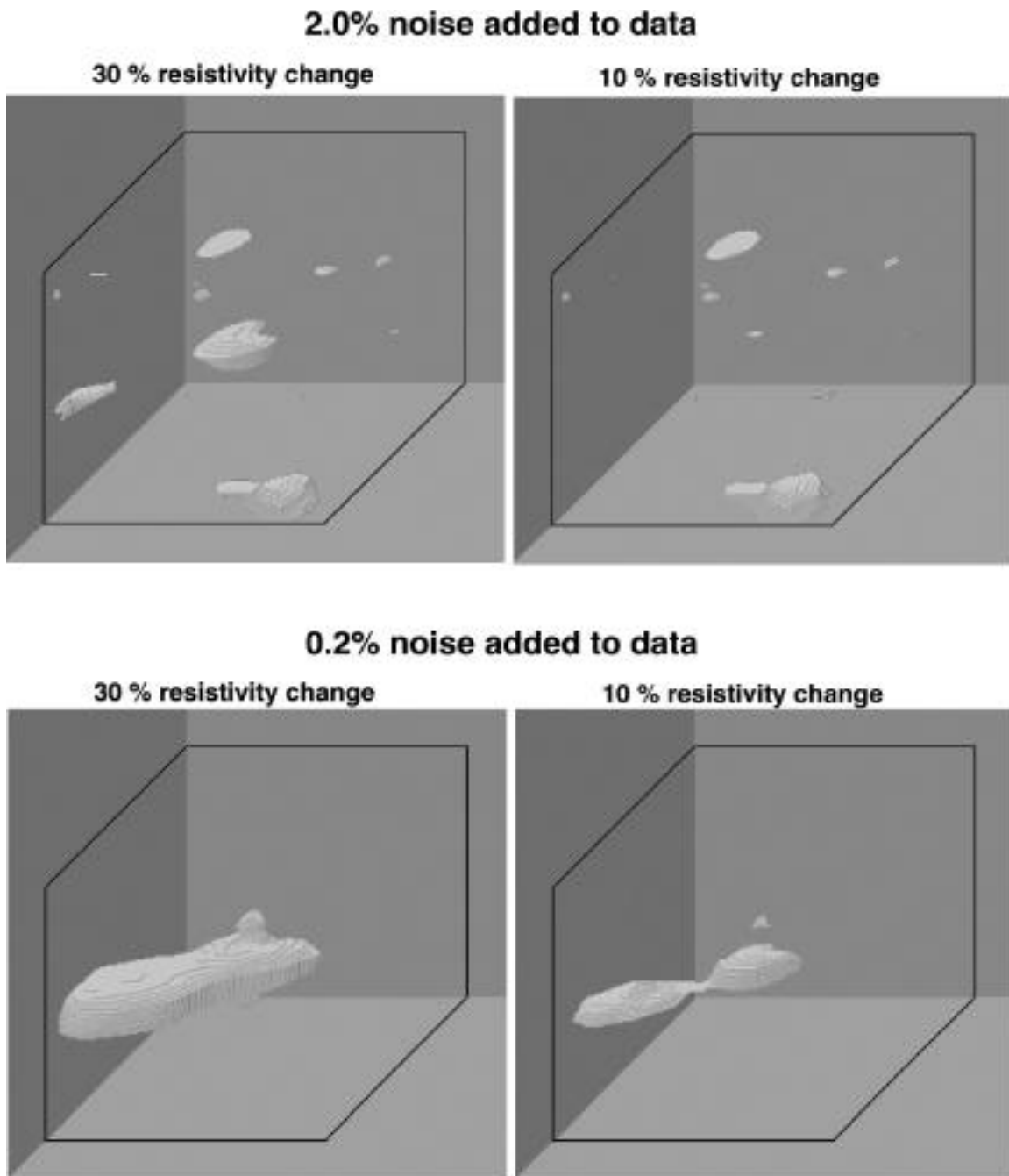


Figure 11 shows point electrode reconstructions for different levels of noise added to the data. The top and bottom rows of images respectively show the results obtained when 2.0% and 0.2% noise were added to the data.

## Plastic pipe used as a target

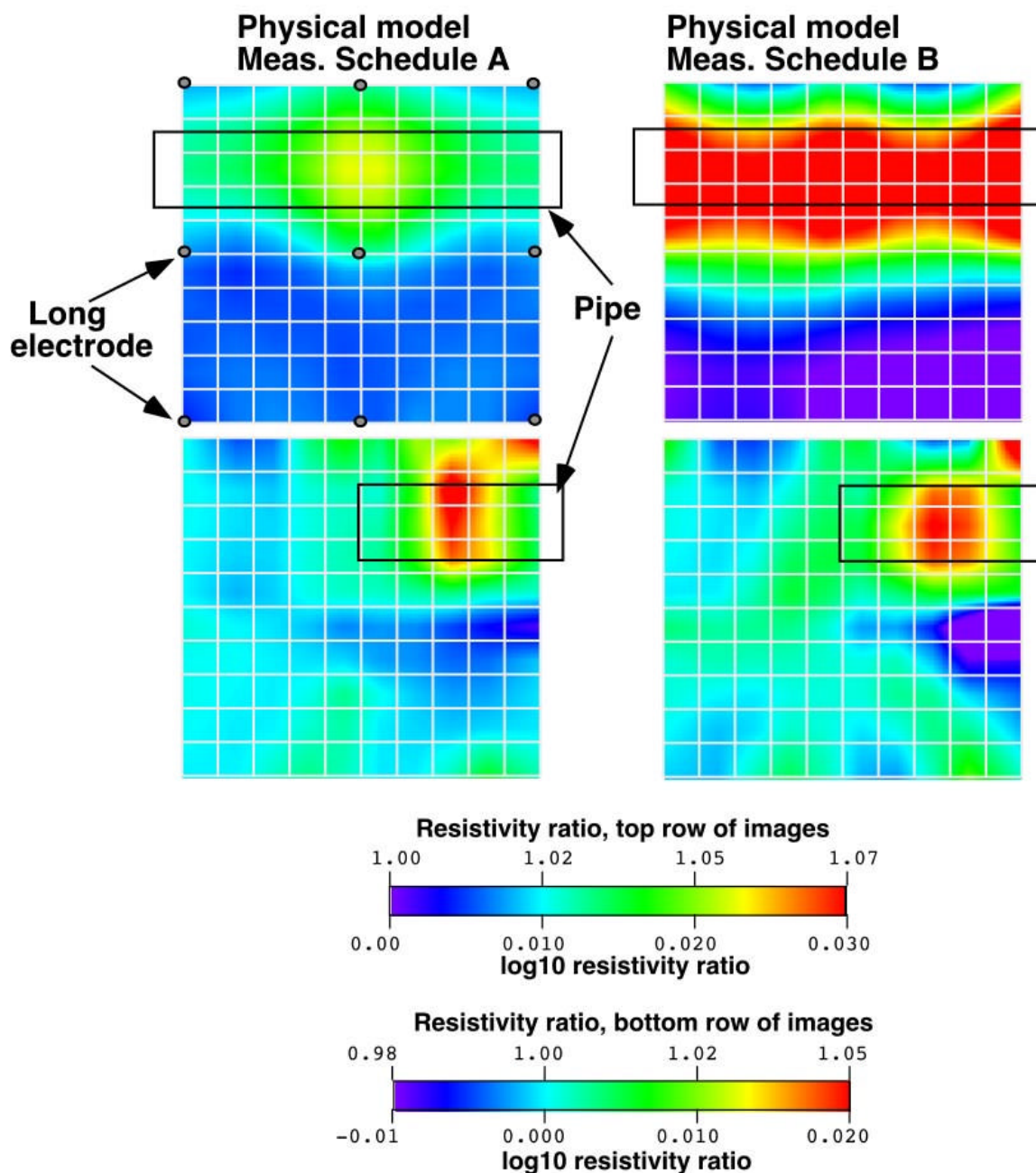
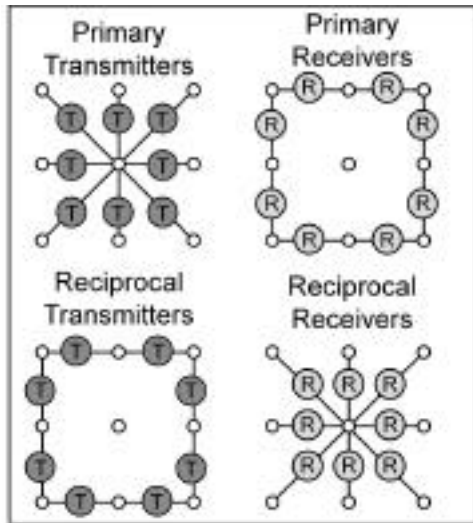
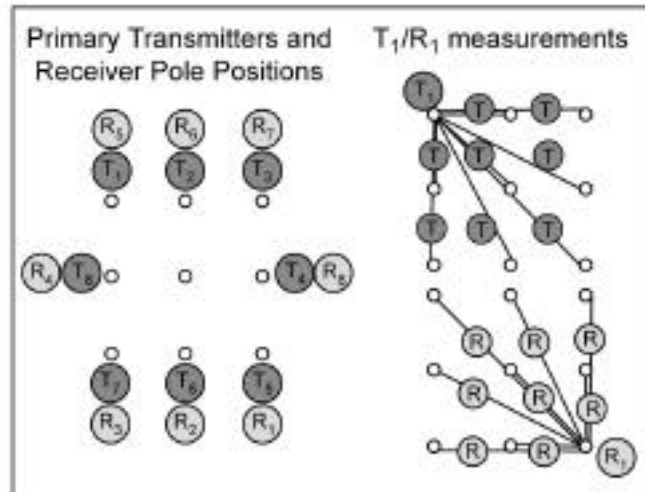


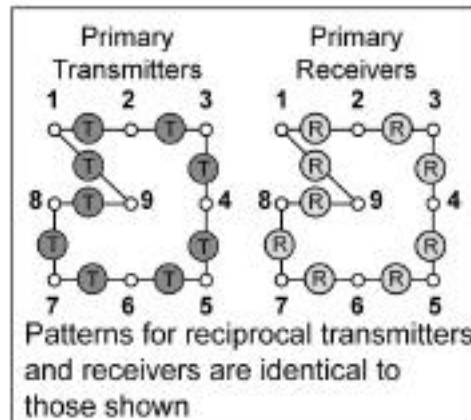
Figure 12 shows long electrode tomographs (plan view) corresponding to a physical model consisting of a plastic pipe immersed in water. The pipe's outline is superimposed on the tomographs. Several measurement schedules were used; here we show the result from two of the better ones.



**Schedule A**  
**(Modified, Symmetric Pole-Pole)**  
 One pole remains fixed, while the other is moved across pattern. All possible combinations, with primary transmitter and receiver poles rotating along the perimeter



**Schedule B (Symmetric Dipole-Dipole):**  
 Complementary combinations of "spoke" and perimeter dipole pairs



**Schedule C**  
**(Asymmetric Dipole-Dipole)**  
 If electrodes are numbered sequentially in the clock-wise manner shown, collect numerically adjacent dipoles

Figure 13 Examples of measurement schedules considered for long electrode surveys. "Measurement schedule" is the sequence of transmitter and receiver dipoles used to measure the electrical properties of a region. The top two diagrams display "symmetric" patterns, whereas the lower diagram does not.

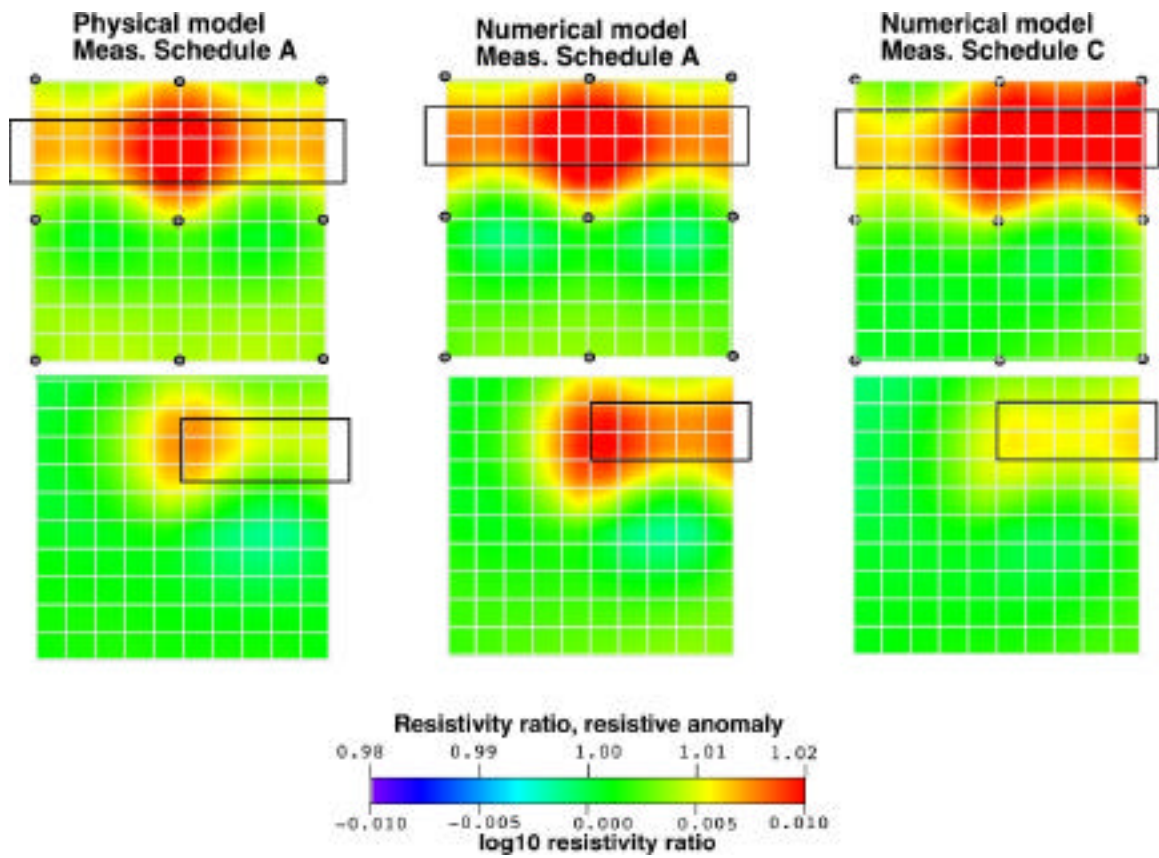
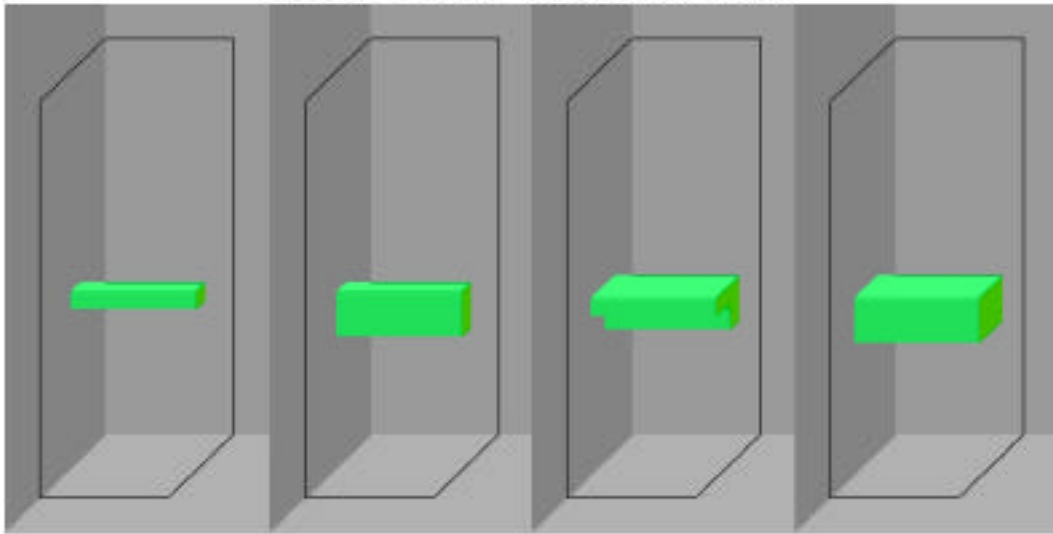


Figure 14 compares long electrode tomographs corresponding to physical and numerical models.

### Plastic foam blocks in a water tank



### Tomographs using point electrode data, resistivity contrast 1.36 : 1 (foam/ water)

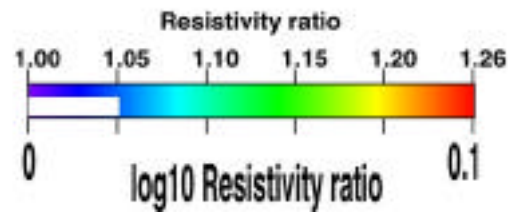
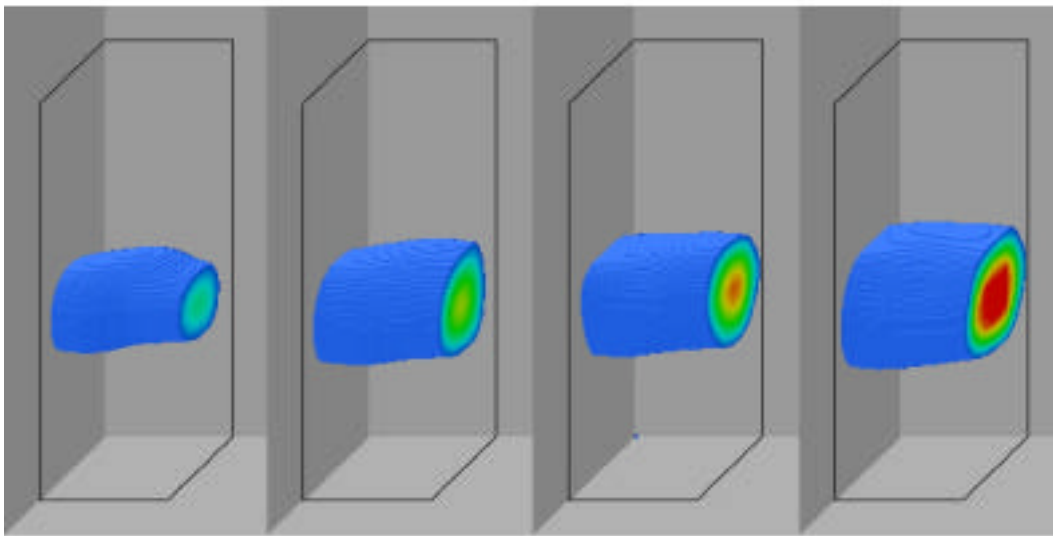


Figure 15 shows point electrode tomographs for a physical model consisting of foam blocks immersed in water. The top row of images shows the physical model configuration. The bottom row shows the tomographs. The white bar superimposed on the color bar indicates the range of transparency values.



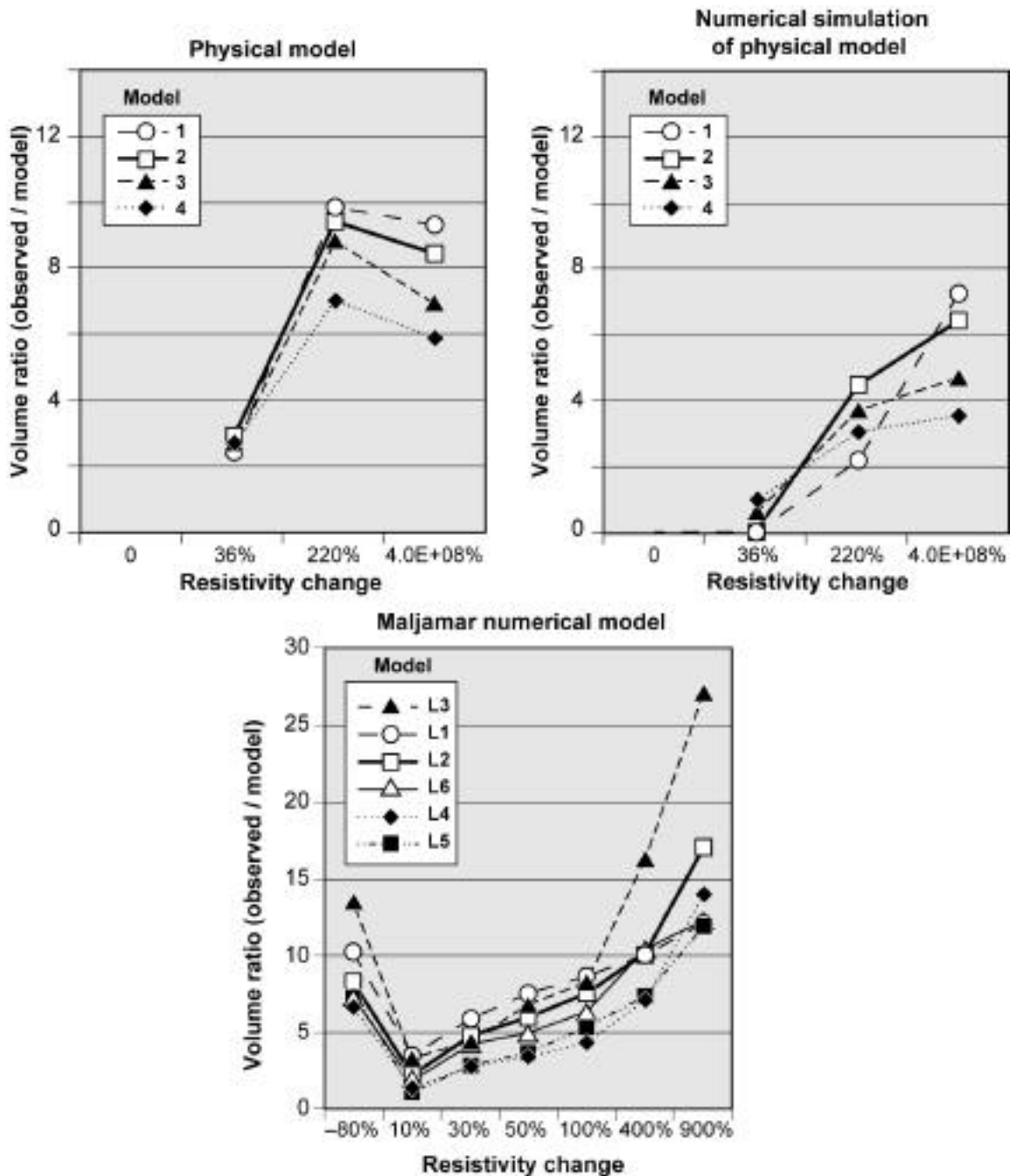


Figure 16 compares volumes ratios corresponding to the foam block physical model, a numerical model based on the foam block model, and the Maljamar numerical model. The volume considered is the volume of the tomograph region that has experienced a change in resistivity  $\geq 10\%$ . Note that the independent variable axis is non-linear.

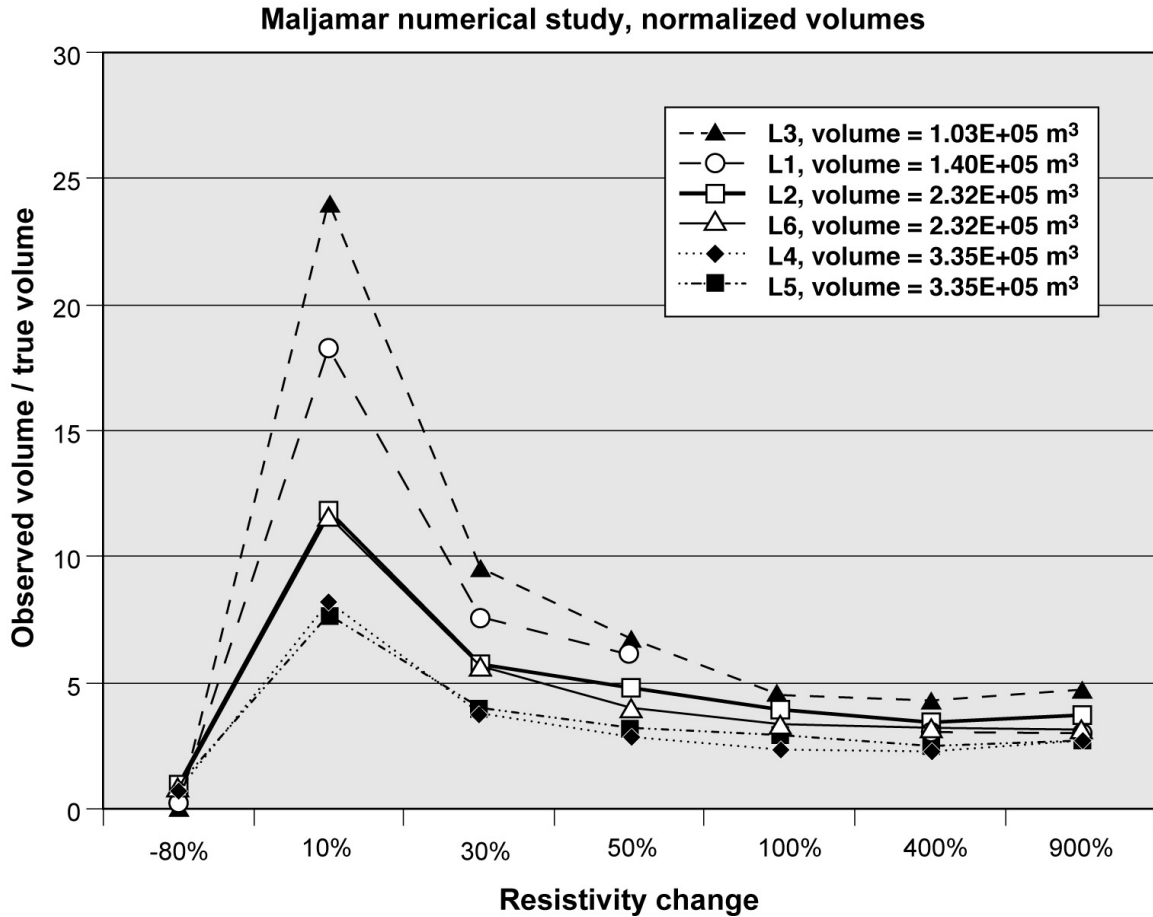


Figure 17 shows the volume estimates for the Maljamar numerical model targets. The volume considered here is the CO<sub>2</sub> fluid volume trapped within the reservoir. Note that the independent variable axis is non-linear. Note that the independent variable axis is non-linear.

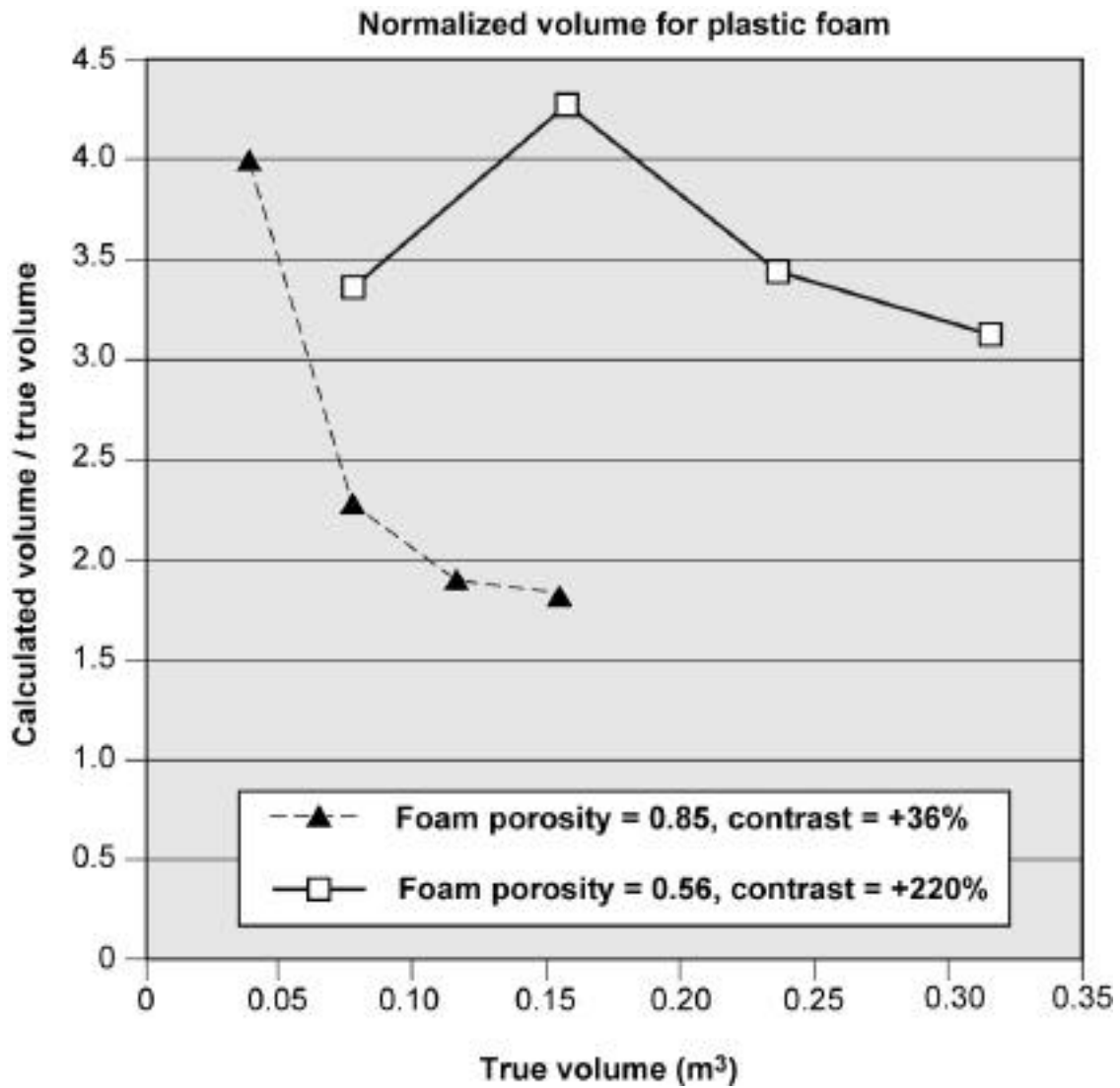


Figure 18 shows the volume estimates for the physical model-foam block targets. The volume considered is solid phase (resistive) volume within the foam block targets. The solid phase is electrically analogous to the CO<sub>2</sub> fluid within a porous reservoir.